 doi:10.20944/preprints202208.0329.v1

Article

Synthetic Aperture Radar Doppler Tomography Detects Undiscovered High-Resolution Internal Structures of the Great Pyramid of Giza

Filippo Biondi [1,*,†,‡], and Corrado Malanga [2]

[1] Department of Electronic and Electrical Engineering, University of Strathclyde, Glasgow G1 1XW, UK;

[2] Department of Chemistry and Industrial Chemistry, University of Pisa Italy, Via Giuseppe Moruzzi, 13, 56100 Pisa, corrado.malanga@unipi.it

* Correspondence: filippo.biondi@marina.difesa.it; Tel.: +39-335-833-4216

† Current address: Via Perella 36, 06073 Corciano (Perugia), Italy

‡ These authors contributed equally to this work.

Abstract: One problem with synthetic aperture radar (SAR) is that, given the limited penetrating effect of electromagnetic waves inside solids, the capability to image inside distributed targets is excluded. Under these circumstances, imaging activity is only given on the surface of distributed targets. This paper describes an imaging approach based on the investigation of micro-movements on the Khnum-Khufu Pyramid, usually generated by background seismic waves. The results obtained prove to be very promising, as high-resolution full 3D tomographic imaging of the pyramid's interior and subsurface was achieved. Khnum-Khufu becomes transparent like a crystal when observed in the micro-movement domain. Based on this novelty, we have completely reconstructed internal objects, observing and measuring structures that have never been discovered before. The experimental results are estimated by processing series of SAR images from the second-generation Italian COSMO-SkyMed satellite system, demonstrating the effectiveness of the proposed method.

Keywords: Synthetic Aperture Radar; Doppler frequencies; multi-chromatic analysis; micro-motion; Pyramid of Khnum-Khufu; sonic images

1. Introduction

The Pyramid of Khnum-Khufu, which is also referred to as the Great Pyramid of Giza or the Pyramid of Cheops, is the most ancient and greatest of the three major pyramids that are included in the necropolis of Giza (Egypt). It is built of granite blocks each weighing about 2.5 tonnes. It is believed that at least two and a half million blocks were required to finish the work, erected with millimetric precision in a relatively short time, estimated at 15 to 30 years [1]. The pyramids of Egypt, although they are one of the most ancient and greatest monuments on Earth, to date there is still no scientifically based, common idea of how they were built [2,3]. The Red Sea was the most prominent harbour structure at the time of King Khufu [4], where an extremely well-preserved harbour compound dating back to the beginning of the Old Kingdom has been excavated at Wadi al-Jarf, along the Egyptian Red Sea coast.

In studying the pyramids' origin, we consider that the ancient mythological writings should not be ignored. A study of the ancient myths and folklore of the world's ancient peoples, which highlights all the many similarities between them, has been conducted in [5]. The claim that myths are unimportant, often considered mere narratives passed down from generation to generation, was discussed. The authors remain open to the hypothesis that a more advanced technological civilisation

 doi:10.20944/preprints202208.0329.v1

might have existed before the known timeline, where the existence of several ice ages prevented the transmission of history. Focusing on the mythical cities referred to in ancient Indian texts, describing how the subcontinent was an integrated element of this [6,7]. However, how the Egyptian pyramids were constructed remained an enduring enigma. A theory that the pyramids were built of cement-like conglomerate, manufactured directly in situ with granular limestone aggregates and an alkaline-silicate binder, is proposed in [8], and evidence is also debated in [9,10]. In order to gain an accurate sense of how the pyramids were made, several engineering theories were examined in [11], noting that in their present form they lay the foundations for new scenarios. At present, the general academic consensus is that the pyramids served as funerary monuments and burial sites for the pharaohs. However, it is also widely analysed that such structures may have been built for a different function. From an aseptic panoramic view, one can find many associations among the pyramids, vibrations and several mechanical devices that resemble hydraulic devices, resonance chambers and acoustic filters [12,13]. The energy to vibrate the pyramids can be provided by the natural environment and the infrasonic vibrations of the Earth's atmosphere can be the source of this energy [14]. This also provides with a framework for the study of specific types of waves, including Lee mountain waves, infrasound, progressive waves in the lower atmosphere, and waves in the upper atmosphere and ionosphere [15]. Atmospheric sound patterns, extended to the combined effects of the ocean at finite depth and source directivity at both elevation and azimuth angles, are studied in [16].

Acoustic waves are widely used in the field of archaeology. The acoustics of three important World Heritage sites such as the five caves in Spain, the Stonehenge stone circle in England and the Paphos Theatre in Cyprus are studied in [17]. Groundwater can influence the geomagnetic field measured in the subsurface. The level of water in the rock determines its electrical conductivity, and thus changes the magnitude of the telluric currents induced in the rock by the change in magnetic fields generated in the ionosphere. This can be studied by using several magnetometers at different points in the subsurface. Geomagnetic signals using two magnetometers were successfully monitored in [18] by setting an optimal electrokinetic magnitude signal upper-bound. A methodology used for self-potential and seismic-electromagnetic measurements, both for on-site and laboratory experiments as well as for modeling is extensively described in [19]. The research also provides the bibliography on studies carried out in hydrology to remotely detect water flows, to deduce their thickness, and to predict their hydraulic conductivity. The observation method discussed also proposes the detection of fractures in wells, which is also useful in trying to study earthquakes. Recent theoretical and experimental studies have produced several unusual and interesting results on the cold fusion of matter experienced on dense lithium [20]. The existence of this exciting propriety of matter relates to zero-point energy estimates that suggest quantum effects play a significant role in shaping the phase diagram of lithium. The vibration-induced property change in the melting and solidifying process of silver nanoparticles with the use of molecular dynamics simulation was found in [21].

The general problem of acoustic wave propagation through parallel paths is addressed by the information theory of two-port telecommunication networks. This allows any mechanical system to be considered as a single element with two gates. Such a circuit is schematically represented with concentrated elements by admittance that have a value compared to the sum of the corresponding instantaneous admittance existing along the parallel paths. In order to calculate all parameters including those representing transmission losses (e.g. the standing wave ratio), in the case of a non-adaptive paths, the theory of transmission lines is well applicable. A Quincke-tube acoustic filter therefore uses two parallel paths. In order to optimize the maximum wave propagation through the system, the Quincke-tube must be adapted and, through the choice of length and thickness of the ducts, can produce a selective transmission loss, so that it can operate as an acoustic filter. In [22], the transmission loss characteristics of several other variations in duct sizes and lengths are presented, together with some very limited experimental data. The phenomenon of pressure pulsations in pipeline systems caused by centrifugal pumps or reciprocating compressors are known to have detrimental effects on industrial applications. An experimental investigation of the attenuation mechanism of

 doi:10.20944/preprints202208.0329.v1

a Herschel-Quincke device and its effectiveness in damping pressure pulsations when applied to a resonant piping system had been presented in [23].

The development of mechanical engineering in ancient Egypt through the stone industry was described in [24], covering the period from the Predynastic to the Old Kingdom. The characteristics and innovations of stone vessels available in these periods were analyzed. Conventional sound absorbers can hardly possess the good performance of low-frequency and broadband absorption simultaneously. In order to combine these two functions into one kind of absorbers, the gradually perforated porous materials backed with Helmholtz resonant cavity are proposed in [25]. A strategy to design three-dimensional elastic periodic structures endowed with complete band-gaps, the first of which is ultra-wide, where the top limits of the first two band-gaps are overstepped in terms of wave transmission in the finite structure is proposed in [26]. Thus, subsequent band-gaps are merged, approaching the behavior of a three-dimensional low-pass mechanical filter.

The debate on how the granite blocks could have been transported up the full height of the pyramids is still an open one. To this end, the theory of in-situ formation of the blocks by means of a cement mixture has also been formulated. Most synthetic stones can be made from re-agglomerated materials. Starting with a mineral substance such as granite rock or naturally eroded, disintegrated or not-aggregated limestone, it is given a compact structure using a binder, such as a geological glue that agglomerates to bond the mineral particles to each other. The result is a new rock with the same mechanical characteristics as a natural equivalent. Such a technique is supposed to have been used to build the pyramid of Khnum-Khufu [8,27].

It has been also studied that the generation of waves of any nature can be also correlated with the brain waves of the living creatures. Previous correlations between geomagnetic activity and quantitative changes in electroencephalographic power revealed interesting associations with the right parietal lobe, compatible with theta activity, and the right frontal region for activity in gamma frequencies. During the experiment [28], subjects were exposed to no magnetic field first, then they were exposed to a purely magnetic field of 20 nT or 70 nT, at a frequency of 7 Hz, with amplitude-modulated signals for 30 minutes. Quantitative electroencephalographic (QEEG) measurements were taken before, during and after exposure and results support the thesis that magnetic field fluctuations are primarily responsible for the significant geomagnetic-QEEG correlations reported in several studies. Studying the effects of weak complex magnetic fields on the neuroplasticity of rats, following the induction of early epilepsy, an unprecedented increase in post-crisis mortality (76%) was observed in young rats that had been exposed perinatally to magnetic fields of 7 Hz with a maximum intensity of about 5 nT. Rats exposed to fields less intense or more intense than this frequency did not show this magnitude of significant mortality [29,30].

Back to the pyramid of Khnum-Khufu, for over a century it has been known that the beams forming the ceiling of the King's Chamber and those of the first and second Relieving Chambers in the Great Pyramid are cracked. However, the temporal origin of these cracks is still unknown. The results of a 3D virtual reality computer simulation designed to determine precisely when the beams cracked are reported in [31]. Several 3D imaging techniques applied on the Khnum-Khufu pyramid are developed in [32]. Among all the theories formulated to try to explain how the pyramid of Khnum-Khufu was built, there is also the hypothesis of the existence of an internal ramp that goes around the pyramid several times. This theory could prove the fact that the pyramid could have been built in twenty years [33]. Microgravity surveys of the Khnum-Khufu pyramid have shown, considering also the general structure of the pyramid. A new interpretation technique for endoscopy of large finite bodies has been developed in [34]. In order to carry out non-invasive internal scans of the pyramid [35], using electromagnetic waves, it is necessary to use special georadar [36], which however have the limitation of having little penetration inside the granite.

The study of ancient Egyptian monuments attracted the attention of experts all over the world. A recent event that confirms this is the discovery, using muon sensors [37,38], of the presence of a previously unknown cavity located inside the pyramid of Khnum-Khufu. Since this discovery cannot

 doi:10.20944/preprints202208.0329.v1

be directly confirmed by drilling, another independent non-destructive method is needed to confirm this discovery and provide an accurate determination of the location and shape of the cavity. A possible holographic radar simulation framework for the detection of openings or other unknown structures of interest is analyzed in [35].

Research [39] for the first time investigated the possibility to use cosmic-ray detectors involved their ability to measure the angle of arrival of penetrating cosmic rays muons with great precision over a large sensitive area. In [40] authors reported the discovery of a large void (with a cross-section similar to that of the Grand Gallery and a minimum length of 30 metres) situated above the Grand Gallery.

The investigation of the microgravimetric measurements on the side of a pyramid could also map the recently discovered "muon chamber" in the Great Pyramid of Khnum-Khufu in Egypt. In[41] the exploitation of technical capabilities of modern gravimeters, is used to perform three-dimensional model calculations with realistic model parameters. A gradiometer survey has been carried out in [42] over a surface area of 100m $\times$ 100m to achieve the purpose and the magnetic data were processed using Geoplot software in order to obtain high quality images of hidden structures inside the Khnum-Khufu pyramid. The results obtained show the presence of interconnected large tomb structures composed of mud-bricks; some other ancient rooms and walls are also present.

A climbing robot called "Djedi" has been designed, constructed, and deployed in [43] to explore shafts of the Queen's chamber within the Great Pyramid. The Djedi robot is based on the concept of inchworm motion and is capable of carrying a long reach drill or snake camera. The robot successfully climbed the southern shaft of the Great Pyramid, deployed its snake camera, and revealed writing not seen for thousands of years. Robot design, including climbing steps in the shaft and lessons learned from experimental deployment, has been designed in [43].

Satellite remote sensing is widely used in the field of archaeology [44,45]. Data from the use of SAR to survey the southern Maya plains suggest that large areas were continuously drained by ancient canals that may have been used for intensive cultivation. In agreement with the authors of [46], SAR remote sensing confirmed the existence of the canals. Through excavations and in-situ ground surveys, they provided sufficient comparative information. Correlating all the data, it was concluded that the Maya civilization, of the Late Classic period, was firmly based on intensive and large-scale cultivation of marshy areas.

Research [47] found an ideal model configuration, associated with spiral ramps, demonstrating how Egyptians could have built the pyramids. In the past, Synthetic Aperture Radar (SAR) vibrations have been very useful in estimating key vessel characteristics. Research [48,49] propose a novel strategy to estimate the micro-motion (mm) of ships from SAR images. The proposed approach is for mm estimation of ships, occupying thousands of pixels, processes the information generated during the coregistration of several re-synthesized time-domain and not overlapped Doppler sub-apertures of COSMO-SkyMed satellite single-look complex (SLC) data. Authors of [50] propose a new procedure to monitor critical infrastructures like the Mosul dam, processing COSMO-SkyMed data. The proposed procedure is an in-depth modal assessment based on the mm estimation, through a Doppler sub-apertures tracking and a multi-chromatic analysis. The procedure described above was made available to perform a comprehensive survey of large road bridges, according to [51]. The authors of [52–54] successfully formulated a comprehensive procedure to perform structural health monitoring using SAR. The technique allows to successfully estimate the position and shape of cracks on bridges in order to prevent their collapse.

In this paper we use a new method based on the tomographic reconstruction of mm, with the aim to perform imaging of the principal targets that make up visible the main internal structure of the pyramid. We use the similar methods already experimented in [50] to search for cracks in large infrastructures, but not for tomography. The physical principle we use is that of estimating the vibrations captured by the Khnum-Khufu pyramid during the SAR observation time interval. The vibration estimation is done by evaluating the Doppler centroid anomalies, an indispensable parameter

Preprints (www.preprints.org) | NOT PEER-REVIEWED | Posted: 18 August 2022 doi:10.20944/preprints202208.0329.v1

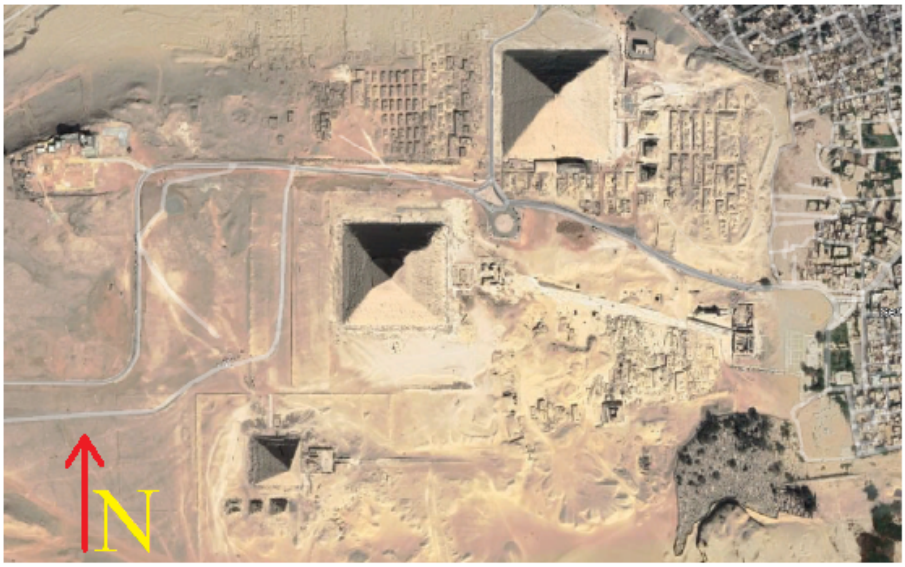

Figure 1. Electro-optical satellite representation of the Giza plateau. The pyramidal infrastructure is visible, oriented to the North.

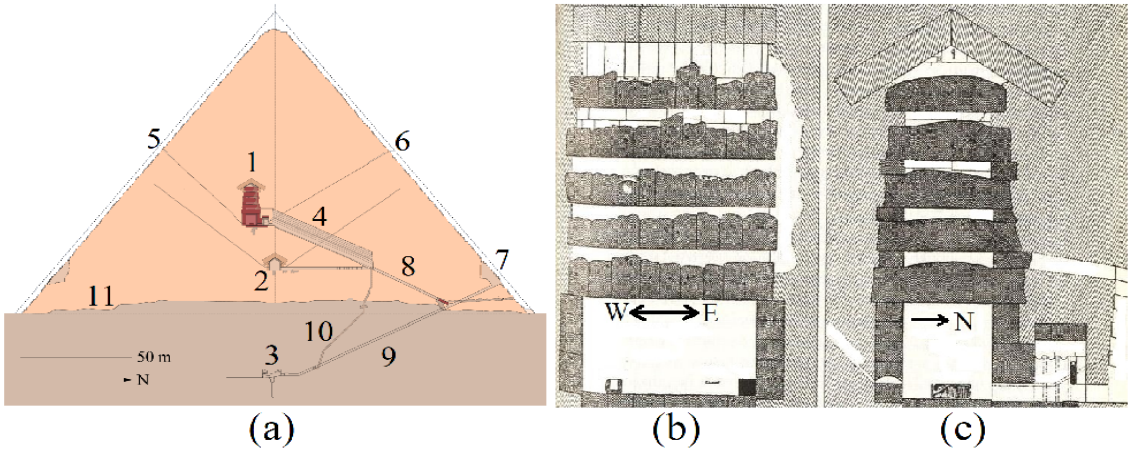

Figure 2. Khnum-Khufu scheme of the known internal structures.

that is used during the SAR azimuth focusing process. We use Doppler sub-apertures to estimate the vibrations present on the pyramid. The vibration energy is generated from many sources such as wind. Great contribution in terms of vibration energy, is also generated by the city of Cairo, which is located closely to the pyramid of Khnum-Khufu and by the presence of Nile river.

We processed several SAR images observed in the Vertical-Vertical (VV) polarization, and the estimated mm allows us to visualize the principal internal components present in the pyramid. We can state that the experimental results we propose definitively solve one of the oldest mysteries of human existence, the complete solution of the internal structure of Khnum-Khufu. To this end, in order to provide a more complete contribution to our work, we have firstly investigated the details of the external structure of all the pyramids belonging to the Giza Plateau (Khufu, Kefren and Menkaure), then we concentrated on studying the internal structure of the pyramid of Khnum-Khufu alone, providing a complete and detailed 3D reconstruction of all the known and unknown chambers, based on tomographic SAR measurements. In the paper, we provide a complete list of the internal structures measured by tomography, each of them marked with a unique sequential number.

 doi:10.20944/preprints202208.0329.v1

Table 1. Characteristics of the SAR acquisitions.

SAR parametrer	Value
Chirp bandwidth	250 MHz
PRF	2 kHz
PRT	0.23 ms
Antenna length	6 m
Type of acquisition	Stripmap
Polarization	HH
Acquisition duration	5 s
Platform velocity	7 km/s
Observation height	650000 m

2. Giza Plateau Presentation and Description

The pyramid of Khnum-Khufu is a monumental structure built mainly of granite blocks, its orientation is almost perfectly aligned to the North. The monumental complex of the Giza plateau is represented in Figure 1. The three pyramids, Khnum-Khufu (top right), Kefren (located in the center) and Menkaure (the last on the bottom left) can be observed. In this context our work focuses on visualizing the vibrational tomographic profile of the pyramid of Khnum-Khufu. The Figure 2 (a) is the schematic representation of the North-south central section of the infrastructure. The figure represents the schematic of what is known and the main parts of the infrastructure are numbered sequentially from 1 to 11. The object consists of the Zed and the King's chamber, with its sarcophagus inside. The Zed, the details of which can be seen in Figure 2 (b) and (c), is a large monument made entirely of granite, consisting of an upper roof made of two oblique granite slabs, and five parallel stone slabs, spaced at varying distances from each other. Each stone has its upper face not smooth, so each surface has a pronounced roughness. On the contrary, each of its lower faces is extremely smooth. Below this monument is the King's room. Boh the Zed and the king's room are off-axis with respect to the apex of the pyramid and are located toward the south on the north-south symmetry plane. Object 2 of Figure 2 (a), is the Queen's room, a smaller volume object located on the axis of the pyramid and below the King's room. As can be seen from the figure 2 (a), Object 2, unlike the King's room, is located exactly under the apex of the pyramid. The last room is Object 3 which is also off-axis of the pyramid, it is also shifted to the south, but in this case, it is located underground. It is usually called the unfinished room. Object 4 represents a large corridor that connects the King's room with the Queen's room, it is called the Grand Gallery. Objects 5, and 6 are air ducts, while the remaining ducts 8, 9, and 10 connect the Grand Gallery with the Queen's room and the unfinished room (the one located below ground). Object 7 is the entrance to the pyramid, and finally, line 11 indicates the surface on which the pyramid sits.

3. Methodology

In this paper, the m-m imaging technique is applied to conduct sonic imaging by processing a single synthetic aperture radar (SAR) image in the single-look-complex (SLC) configuration. The method includes the m-m estimation that belongs to the Khnum-Khufu pyramid and is caused by the background ripple of subsurface seismic activity that reflects surface vibrations. The m-m is estimated by means of MCA, carried out in the Doppler direction. Several Doppler sub-apertures, SAR images with lower azimuthal spatial resolution, are generated to evaluate the vibrational trend of specific pixels of interest. The infrachromatic displacement is measured through the pixel tracking technique [48,49], using a high-performance sub-pixel coregistration [52,57]. The vibrations measured in the direction of the tomographic view, embedded in multi-chromatic Doppler diversity, are focused along the height (or depth) dimension and produce high-resolution tomographic images of the subsurface.

The SAR synthesizes the electromagnetic image through a "side looking" acquisition, according to the observation geometry shown in Figure 3, where:

Preprints (www.preprints.org) | NOT PEER-REVIEWED | Posted: 18 August 2022 doi:10.20944/preprints202208.0329.v1

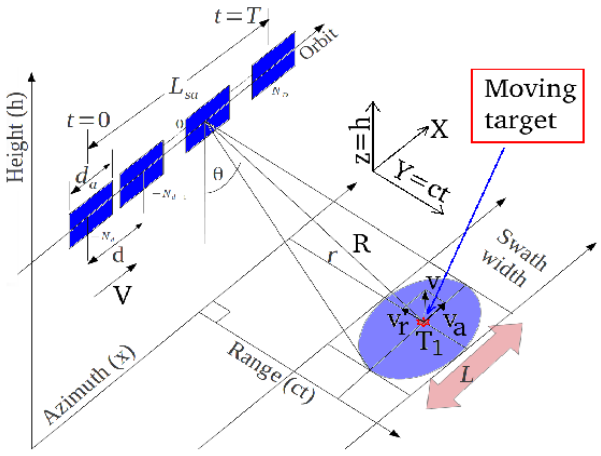

Figure 3. SAR acquisition geometry.

- Zero-Doppler distance r (constant);
- Slant-range R;
- Reference range R_0, at $t = 0$;
- Physical antenna aperture length d_a;
- Platform velocity V;
- Distance between two range acquisitions d;
- Total synthetic aperture length G_{sa};
- Acquisition time variable t;
- Observation duration T;
- Start and stop time acquisition $t = 0$ and $t = T$ respectively;
- Azimuth electromagnetic footprint width $L = \frac{\lambda r}{d_a}$;
- Electromagnetic radiation pattern incidence angle θ.

All the parameters mentioned above are connected to the fixed-light SAR imaging used in this work. SAR data that belongs to the electromagnetic image are generated through the focusing process that involves the application of a two-dimensional matched filter that acts in the range and azimuth direction. For each event N_i for $i = -N_d, \ldots, N_d$ The SLC signal resulting from compression is given by [55]:

$$s_{SLC}(k,x) = 2N\tau \exp\left[-\jmath\frac{4\pi}{\lambda}r\right] \operatorname{sinc}\left[\pi B_{c_r}\left(k - \frac{2R}{c}\right)\right] \operatorname{sinc}\left[\pi B_{c_D} x\right]$$
$$\text{for } x = kt,\ k = \{0,1,\ldots,N-1\},\ x = \{0,1,\ldots,M-1\},\ \text{with } N, M\ \in \mathbb{N}. \tag{1}$$

Equation (1) represents the focused SAR signal generated by the back-scattered electromagnetic energy of a point target supposed to be stationary. The terms B_{c_r}, and $B_{c_D} = \frac{4Nd}{\lambda r}$ are the total chirp and Doppler bandwidths respectively. The total synthetic aperture is equal to $L_{sa} = 2Nd$ and the azimuth resolution $\delta_D \approx \frac{1}{B_{c_D}} = \frac{\lambda R}{2L_{sa}}$. In (1) the $\frac{2\vec{R}}{c}$ parameter identifies the position in range where the maximum of the sinc function is positioned, while in azimuth it is centered around "zero". In the case where the peak of the sinc function has a nonzero coordinate along the azimuth dimension, Equation (1) can be recast as:

$$s_{SLC}(k,x) = 2N\tau \exp\left[-\jmath\frac{4\pi r}{\lambda}\right] \operatorname{sinc}\left[\pi B_{c_r}\left(k - L_{c_g}\right)\right] \operatorname{sinc}\left[\pi B_{c_D}\left(x - L_{D_h}\right)\right]$$
$$\text{for } L_{c_g},\ L_{D_h}\ \in \mathbb{N}, \tag{2}$$

Preprints (www.preprints.org) | NOT PEER-REVIEWED | Posted: 18 August 2022 doi:10.20944/preprints202208.0329.v1

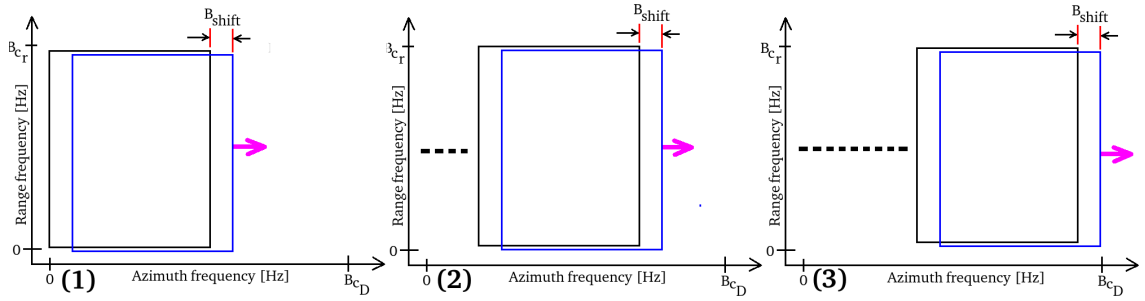

Figure 4. Doppler sub-apertures.

where the DFT is equal to:

$$\begin{aligned} S_{SLC_F}(n,q) &= DFT2\left\{2N\tau\exp\left[-\jmath\frac{4\pi r}{\lambda}\right]\operatorname{sinc}\left[\pi B_{c_r}k\right]\operatorname{sinc}\left[\pi B_{c_D}x\right]\right\} \\ &= 2N\tau\exp\left[-\jmath\frac{4\pi r}{\lambda}\right]\sum_{k=0}^{N-1}\sum_{x=0}^{M-1}\operatorname{sinc}\left[\pi B_{c_r}n\right]\operatorname{sinc}\left[\pi B_{c_D}q\right] \\ &e^{\left(-\jmath\frac{2\pi kn}{N}\right)}e^{\left(-\jmath\frac{2\pi xq}{M}\right)} \\ &= 2N\tau\exp\left[-\jmath\frac{4\pi r}{\lambda}\right]\frac{1}{\pi B_{c_r}}\Pi\left[\frac{n}{\pi B_{c_r}}\right]\frac{1}{\pi B_{c_D}}\Pi\left[\frac{q}{\pi B_{c_D}}\right] \\ &e^{\left(-\jmath 2\pi nL_{c_g}\right)}e^{\left(-\jmath 2\pi qL_{D_h}\right)}, \end{aligned} \tag{3}$$

which has a rectangular shape.

3.1. Model of the Doppler Sub-Apertures

In this paper, we test a new strategy that employs Doppler sub-apertures, generated to measure the movement of the target. Figure 4 depicts the bandwidth allocation strategy used. From the single SAR image, we compute the 2D digital Fourier transform (DFT), which, in accordance with (3), takes a rectangular form. As we can observe from Figure 4, B_{C_D} is the total Doppler waveband we synthesised with the SAR observation, while $B_{D_L} = \frac{B_{C_D}}{2}$ is the bandwidth that we left outside the limits of the matched filter, to get enough sensitivity to predict the target's motion. Here, the formula 3 is the focused SAR spectrum, at the highest resolution, exploiting the entire band B_{c_r}, B_{C_D}, according to the frequency allocation strategy shown in Figure 4, the following range-Doppler sub-aperture matrix is built for multidimensional Master information:

$$\begin{aligned} &S_{SLC}(k,x)_M = \left[S_{SLC}(k,x)_{M_{\{1,1\}}} \quad S_{SLC}(k,x)_{M_{\{1,2\}}} \quad S_{SLC}(k,x)_{M_{\{1,3\}}} \quad \dots \quad S_{SLC}(k,x)_{M_{\{1,N_D\}}}\right] \\ &\text{for } N_D \in \mathbb{N}, \end{aligned} \tag{4}$$

and for the slave, the following large-matrix is presented:

$$\begin{aligned} &S_{SLC}(k,x)_S = \left[S_{SLC}(k,x)_{S_{\{1,1\}}} \quad S_{SLC}(k,x)_{S_{\{1,2\}}} \quad S_{SLC}(k,x)_{S_{\{1,3\}}} \quad \dots \quad S_{SLC}(k,x)_{S_{\{1,N_D\}}}\right] \\ &\text{for } N_D \in \mathbb{N}, \end{aligned} \tag{5}$$

The following explanation of the chirp-Doppler sub-aperture approach, shown in Figure 4, is given: Consider Figure 4, where the master and slave sub-bands are determined by focusing the SAR image, in which the matched filter sets to exploit a range-azimuth bandwidth equal to

Preprints (www.preprints.org) | NOT PEER-REVIEWED | Posted: 18 August 2022 doi:10.20944/preprints202208.0329.v1

$B_{c_r}, B_{c_D} - B_{D_L}$. The not processed bandwidths B_{D_L} are divided into N_D equally distributed bandwidth steps respectively. At this point N_c rigid shifts of the master-slave system along the azimuthal bandwidth domain are performed in order to populate the entire row of 4 and 5. The procedure is repeated N_D times for every azimuth shift, in fact, the figures 4 (1), (2) and (3), represent the azimuth frequency variation strategy when the Doppler bandwidth is at N_D. At every Doppler frequency displacement $\frac{B_{c_D} - B_{D_L}}{N_D}$ we populate all elements of 4 and 5.

3.2. Description of the Doppler Sub-Aperture

The decomposition of the SAR data into Doppler sub apertures is formalized in this subsection, which is performed starting from the spectral representation of the focused SAR data. To this end, notice that the generic $i-$th chirp sub-aperture 2-dimensional DFT of (2) is given by:

$$\begin{aligned} S_{SLC_{F_i}}(n,q) &= DFT2\left\{2N\tau \exp\left[-\jmath\frac{4\pi r}{\lambda}\right]\frac{\sin\left[\pi B_{c_{r_i}}\left(k-L_{c_g}\right)\right]}{\left[\pi B_{c_{r_i}}\left(k-L_{c_g}\right)\right]}\cdot\frac{\sin\left[\pi B_{c_D}\left(x-L_{D_h}\right)\right]}{\left[\pi B_{c_D}\left(x-L_{D_h}\right)\right]}\right\} \\ &= 2N\tau\exp\left[-\jmath\frac{4\pi r}{\lambda}\right]\sum_{k=0}^{N-1}\sum_{x=0}^{M-1}\cdot\frac{\sin\left[\pi B_{c_{r_i}}\left(n-L_{c_g}\right)\right]}{\left[\pi B_{c_{r_i}}\left(n-L_{c_g}\right)\right]}\cdot\frac{\sin\left[\pi B_{c_D}\left(q-L_{D_h}\right)\right]}{\left[\pi B_{c_D}\left(q-L_{D_h}\right)\right]} \\ &\quad e^{\left(-\jmath\frac{2\pi kn}{N}\right)}\cdot e^{\left(-\jmath\frac{2\pi xq}{M}\right)} \\ &= 2N\tau e^{\left[-\jmath\frac{4\pi r}{\lambda}\right]}\frac{1}{\pi B_{c_{r_i}}}\Pi\left[\frac{n}{\pi B_{c_{r_i}}}\right]\frac{1}{\pi B_{c_D}}\Pi\left[\frac{q}{\pi B_{c_D}}\right]e^{\left(-\jmath 2\pi n L_{c_g}\right)}\cdot e^{\left(-\jmath 2\pi q L_{D_h}\right)}. \end{aligned} \tag{6}$$

From the last equation, it turns out that a single point stationary target has a two-dimensional rectangular nature with total length proportional to the range-azimuth bandwidths respectively. The phase term $\exp\left(-\jmath 2\pi n L_{c_g}\right)\exp\left(-\jmath 2\pi q L_{D_h}\right)$ is due to the sinc function dislocation in range and azimuth when the SLC SAR data are considered. In the SAR, the movement of a point target with velocity in both range and azimuth direction is immediately warned by the focusing process, resulting in the following anomalies:

- azimuth displacement when target constant range velocity is present;
- azimuth smearing when target azimuth velocity or target range accelerations are present;
- range defocusing caused by range-walking phenomenon, when target range speed is present, backscattered energy is detected among several range resolution cells.

In practical cases, the backscattered energy from moving targets is distributed over several range-azimuth resolution cells. As a matter of fact, considering the point-like target T_1 (of Figure 3) that is moving with velocity $\vec{v}_t$ whose range-azimuth and acceleration components are $\{v_r, v_a\}$, and $\{a_r, a_a\}$, respectively, then we can write

$$\begin{aligned} &R^2(t) = (Vt - S_a)^2 + (R_0 - S_r)^2 \text{ with } S_r = v_r t + \frac{1}{2}a_r t^2 \text{ and } S_a = v_a t + \frac{1}{2}a_a t^2 \\ &|R(t)| = |R_0 - S_r|\left\{1 + \frac{(Vt - S_a)^2}{(R_0 - S_r)^2}\right\}^{\frac{1}{2}}. \end{aligned} \tag{7}$$

We now show the following Taylor expansion:

$$(1+x)^{\beta} \approx 1 + \beta x \tag{8}$$

Preprints (www.preprints.org) | NOT PEER-REVIEWED | Posted: 18 August 2022 doi:10.20944/preprints202208.0329.v1

and that $R_0 - S_r \approx R_0$, and $(V_t - S_a)^2 \approx V^2t^2 - 2VtS_a$, (7) can be written in the following form:

$$|R(t)| = \left\{ \frac{1}{2} \frac{(Vt - S_a)^2}{(R_0 - S_r)} + |R_0 - S_r| \right\} = |R_0 - S_r| + \left(1 - \frac{2S_a}{Vt}\right) \cdot \frac{V^2t^2}{2R_0} \tag{9}$$

$$\begin{aligned} &= R_0 + \frac{V^2t^2}{2R_0} - \frac{VtS_a}{R_0} - S_r \\ &= R_0 + \frac{V^2t^2}{2R_0} - \frac{Vt\left(v_at + \frac{1}{2}a_at^2\right)}{R_0} - v_rt - \frac{1}{2}a_rt^2 \\ &= R_0 + \frac{V^2t^2}{2R_0} - \frac{Vv_at^2}{R_0} - \frac{Va_at^3}{2R_0} - v_rt - \frac{1}{2}a_rt^2. \end{aligned} \tag{10}$$

The term $\frac{Va_at^3}{2R_0}$ is neglected and approximated to $\left(V^2 - 2Vv_a\right) \approx (V - v_a)^2$ Equation (10) is:

$$|R(Vt)| = R_0 - v_rt + \frac{t^2}{2R_0}\left[(V - v_a)^2 - R_0a_r\right]. \tag{11}$$

recasting (11) in terms of $x = Vt$, we obtain [56]:

$$|R(x)| = R_0 - \epsilon_{r_1}x + \left[(1 - \epsilon_{c_1})^2 - \epsilon_{r_2}\right]\frac{x^2}{2R_0},\ x = Vt. \tag{12}$$

where:

- $\epsilon_{r_1} = \frac{v_r}{V}$ (generated by velocity in range);
- $\epsilon_{r_2} = \frac{a_rR_0}{V^2}$ (generated by the acceleration in the range component);
- $\epsilon_{c_1} = \frac{v_c}{V}$ (generated by the azimuth velocity).

Thus, the above terms interacts with the received signal, as shown in [56], and formalized in Equation (6) .

4. Model of the Tomographic Method

Taking a single SLC image to which MCA is applied following the frequency allocation strategy shown in Figure 4, we calculate the tomogram depicted by the line of adjacent pixels illustrated in Figure 5. Vibrations are assessed on the tomographic surface spanning from the earth's surface to a depth of several kilometres. The figure represents a series of harmonic oscillators embedded on each pixel of the tomographic line, which are symbolically represented as a spring attached to a mass that oscillates by the application of harmonic vibrations. Any wave generated by each harmonic oscillator rebounds off the Earth's surface when there is an abrupt variation in the medium's density (the earth-air boundary). A vibrational phasor is observed on each pixel over time by applying the MCA Doppler [52,57]. Thanks to the orbital view change (which is conducted in azimuth), an effective deep subsurface vibrational scan of the Earth is achieved.

4.1. Vibrational Model of the Earth

The vibrational model proposed for the Earth's surface is illustrated in Figures 5 (a) and (b). The geometrical reference system for the two figures is the three-dimensional range, azimuth and altitude space. In this case, the height represents the depth below the topographic level (in this particular instance, the limit of the medium is the green plane). The tomographic line of interest is the series of adjacent pixels that lie on the green plane. A mass is hung on each pixel in the tomographic line by means of a spring, as shown in Figure 5 (a). This is now forced to oscillate harmonically, supported by the earth's magma instability. Such oscillations are schematically shown as the vibrational energy

Preprints (www.preprints.org) | NOT PEER-REVIEWED | Posted: 18 August 2022 doi:10.20944/preprints202208.0329.v1

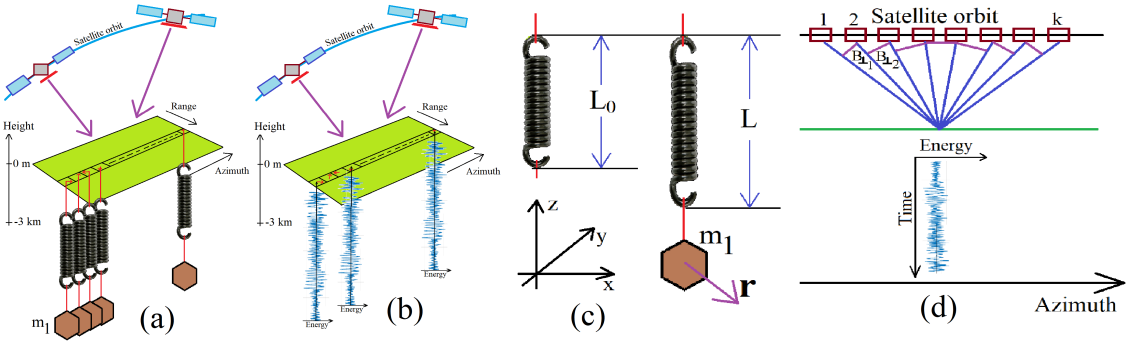

Figure 5. Geometry of the tomographic acquisition.

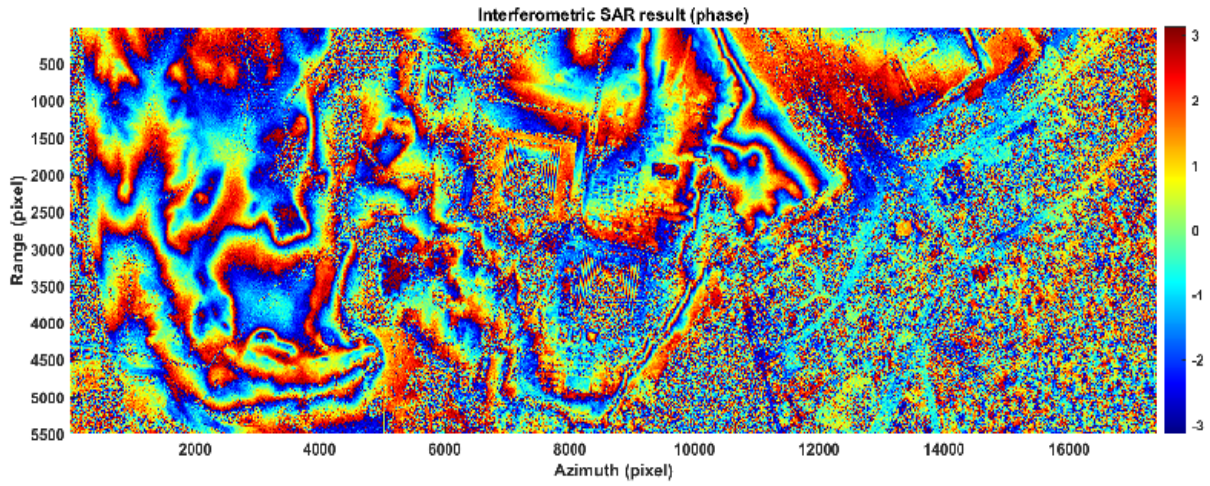

Figure 6. Interferometric repeat-pass phase-map of the Giza plateau.

function visible in Figure 5 (b). The radar instantaneously detects this coherent harmonic fluctuation here. Mathematically, the Earth's displacement is detected as a complex displacement belonging to each pixel of interest. Every instantaneous movement is estimated between the master image and the slave image, where the displacements are evaluated by means of the pixel tracking technique. The number of independent tomographic looks (which depends on the total number of Doppler sub-apertures) is defined by the parameter *k*.

Now suppose the spring is perturbed by an impulsive force. According to this perturbation the string starts to vibrate by describing a harmonic movement (we do not consider any form of friction here). The resulting perturbation will drive the spring through space-time in the form of a sinusoidal function. The seismic wave will therefore reach a constrained terminal, which causes it to reflect in the opposite direction. The reflecting wave will then reach the opposite constraint which will cause it to be reflected in the original direction and back to its original location, keeping the same frequency and amplitude. According to the Classical Physics principles, the rebound wave overlaps the arrival wave so that the interference between two sine waves having the same amplitude and frequency and propagating in opposite directions leads to the generation of an ideal, perpetual stationary wave on the spring. Any vibrational channel is now taken into account when the spring can oscillate in three-dimensional space, in accordance with a particular nature of perturbation. When the Earth is vibrating, it occurs that the spring's length has to oscillate as well. This causes oscillations in the tension domain of the spring. It is clear that these oscillations (i.e. the longitudinal ones) are propagated at approximately twice the frequency of the transverse vibrations. The coupling between transverse and longitudinal oscillations of the spring can be essentially modelled by means of non-linear phenomena. Figure 5 (c, d) illustrates the oscillating model in the Euclidean space-time coordinates (x,y,z,t), where the satellite motion has been purified from any orbital distortions, so that the geometric parameters

Preprints (www.preprints.org) | NOT PEER-REVIEWED | Posted: 18 August 2022 doi:10.20944/preprints202208.0329.v1

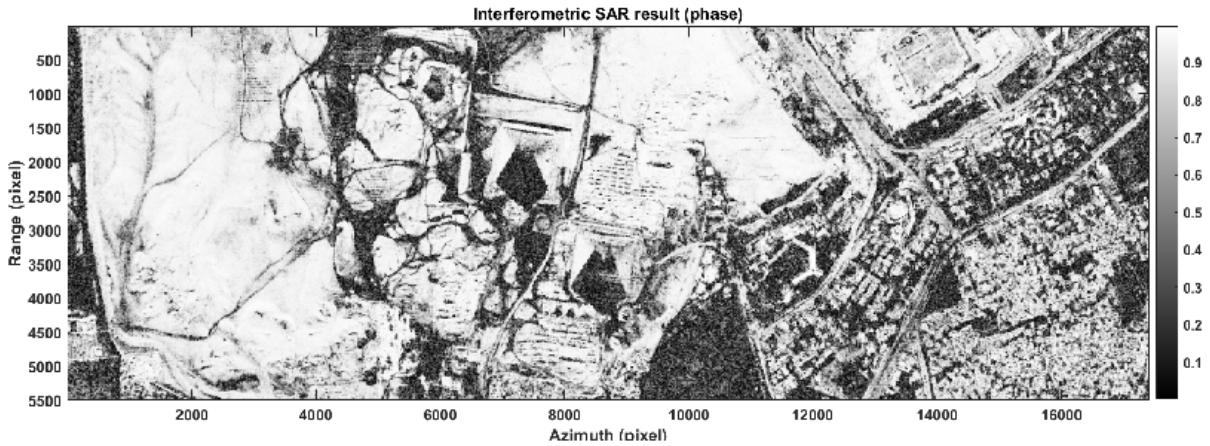

Figure 7. Interferometric repeat-pass coherence of the Giza plateau.

used to perform the tomographic focusing can be rigorously understood. From Figure 5 (c), L is the length of the spring when it is at its maximum tension while L_0 is its length when no mass is present. Finally the spring has been considered to have an elastic constant equal to ξ. The vibrational force applied to the mass $m1$ of Figure 5 (c) is equal to [58]:

$$F = -4\xi \mathbf{r}\left(1 - \frac{L_0}{\sqrt{L^2 + 4\mathbf{r}^2}}\right). \tag{13}$$

If $\mathbf{r} \ll L$, (13) is expanded in the following series:

$$F = -8\xi L_0\left[\left(\frac{\mathbf{r}}{L}\right)^3 - \left(\frac{\mathbf{r}}{L}\right)^5 + \ldots\right] - 4\xi\mathbf{r}(L - L_0)\left(\frac{\mathbf{r}}{L}\right), \tag{14}$$

where a precise approximation of (14) is the following cubic restoring force:

$$F = m\ddot{\mathbf{r}} \approx -4\xi\mathbf{r}(L - L_0)\left[1 + \frac{2L_0}{(L - L_0)}\left(\frac{\mathbf{r}}{L}\right)^2\right]\left(\frac{\mathbf{r}}{L}\right). \tag{15}$$

Considering (15), the non-linearity dominates when $L \approx L_0$. If we define:

$$\omega_0 = \frac{4\xi}{m}\left[\frac{(L - L_0)}{L}\right], \tag{16}$$

and

$$\xi = \frac{2L_0 \cdot (L - L_0)}{L^2}. \tag{17}$$

Considering (15) we have:

$$\ddot{\mathbf{r}} + \omega^2\mathbf{r}\left(1 + \xi\mathbf{r}^2\right) = 0. \tag{18}$$

If we consider damping and forcing (18) is modified as:

$$\mathbf{f}(\omega t) = \ddot{\mathbf{r}} + \lambda\dot{\mathbf{r}} + \omega^2\left(1 + \xi\mathbf{r}^2\right)\mathbf{r}, \tag{19}$$

Preprints (www.preprints.org) | NOT PEER-REVIEWED | Posted: 18 August 2022 doi:10.20944/preprints202208.0329.v1

where $\mathbf{f}(\omega t)$ is the forcing term and λ is the damping coefficient. If non-linearity of (19) is sufficiently low, it can be reduced into the following two-degree-of-freedom linear harmonic oscillator:

$$\mathbf{r}(t) = e^{\left(\frac{-\lambda t}{2}\right)} \cdot (a\cos\omega_0 t, b\sin\omega_0 t)\,. \tag{20}$$

In 20 $\{a, b\}$ are the instantaneous shifts estimated by the coregistrator. The harmonic oscillator (20) is the displacement parameters $\epsilon_{r_1}, \epsilon_{r_2}, \epsilon_{c_1}$ estimated by (12). According to Figure 5 (d) the vector representation of k samples of the time-domain function (20) consisting in the following multi-frequency data input is considered:

$$\mathbf{Y} = [\mathbf{y}(1), \ldots, \mathbf{y}(k)]\,, \in \mathbf{C}^{k\times 1}. \tag{21}$$

The steering matrix $\mathbf{A}(z) = [\mathbf{a}(z_{min}), \ldots, \mathbf{a}(z_{MAX})]$, $\in \mathbf{C}^{k\times F}$ contains the phase information of to the Doppler frequency variation of the sub-aperture strategy, associated to a source located at the elevation position $\mathbf{z} \in \{z_{min}, z_{MAX}\}$,

$$\mathbf{A}(\mathbf{K}_z, \mathbf{z}) = \begin{bmatrix} 1, e^{(\jmath 2\pi k_{z_2} t z_0)}, \ldots, e^{(\jmath 2\pi k_{z_{k-1}} t z_0)} \\ 1, e^{(\jmath 2\pi k_{z_2} t z_1)}, \ldots, e^{(\jmath 2\pi k_{z_{k-1}} t z_1)} \\ \cdots \\ 1, e^{(\jmath 2\pi k_{z_2} t z_{F-1})}, \ldots, e^{(\jmath 2\pi k_{z_{k-1}} t z_{F-1})} \end{bmatrix}, \tag{22}$$

where $\mathbf{K}_z = \frac{4\pi B_\perp}{\lambda \mathbf{r}_i \sin\theta}$, $i = 1, \ldots, k$, $B_\perp$ is the $i-$th orthogonal baseline which is visible in Figure 5 (d), and $\mathbf{r}_i$ is the $i-$th slant-range distance. The standard sonic tomographic model is given by the following relation:

$$\mathbf{Y} \quad = \mathbf{A}(\mathbf{K}_z, \mathbf{z})\mathbf{h}(\mathbf{z}). \tag{23}$$

where in (23) $\mathbf{h}(\mathbf{z}) \in \mathbf{C}^{1\times F}$, inverting (23) I finally find the following tomographic solution:

$$\mathbf{h}(\mathbf{z}) \quad = \mathbf{A}(\mathbf{K}_z, \mathbf{z})^{\dagger}\mathbf{Y}. \tag{24}$$

In the (24) the steering matrix $\mathbf{A}(\mathbf{K}_z, \mathbf{z})$ represents the best approximation of a matrix operator performing the digital Fourier transform (DFT) of $\mathbf{Y}$. The tomographic image $\mathbf{h}(\mathbf{z})$, which represents the spectrum of $\mathbf{A}(\mathbf{K}_z, \mathbf{z})$, is obtained by doing pulse compression.

The tomographic resolution is $\delta_T = \frac{\lambda R}{2A}$, where R is the slant range, λ is the wavelength of the vibrations present over the Earth, and A is the orbit aperture considered in the tomographic synthesis, in other words, consists to the Doppler bandwidth synthesized to produce the sub-apertures. The maximum tomographic resolution is obtained using this SLC data, synthesized using 24 kHz, is as follows. Considering an average speed of the seismic waves propagation set at $v \approx 6000\frac{m}{s}$, an investigation frequency set to 12500 Hz, the wavelength of these vibrations is $\lambda = \frac{v}{f} \approx \frac{6000}{12500} \approx 0.48m$. Considering all above parameters, the maximum orbital aperture is equal to half the total length of the orbit, therefore about 42000 m. If we set $R = 650000m$ the maximum tomographic resolution is equal to $\delta_z = \frac{\lambda R}{2A} = \frac{0.48\cdot 650000}{2\cdot 42000} \approx 3.71m$. This is the tomographic resolution set to calculate all the experimental parts shown in section 5.

5. Measurements

In this section we will show all the experimental results that have been made and have been divided into external, and internal, measurement results. In the first case, we show the results provided by SAR interferometry (InSAR). These consist of the evaluation of radar interferometric fringes to demonstrate the actual shapes of the outer facades of all pyramids in the Giza Plateau. The

Preprints (www.preprints.org) | NOT PEER-REVIEWED | Posted: 18 August 2022 doi:10.20944/preprints202208.0329.v1

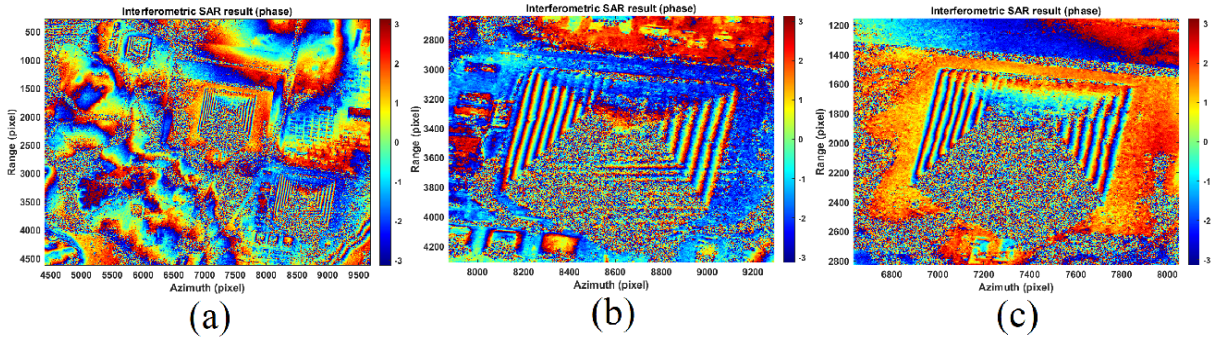

Figure 8. Interferometric satellite representation of the Giza plateau. The pyramidal infrastructure is visible, oriented to the North.

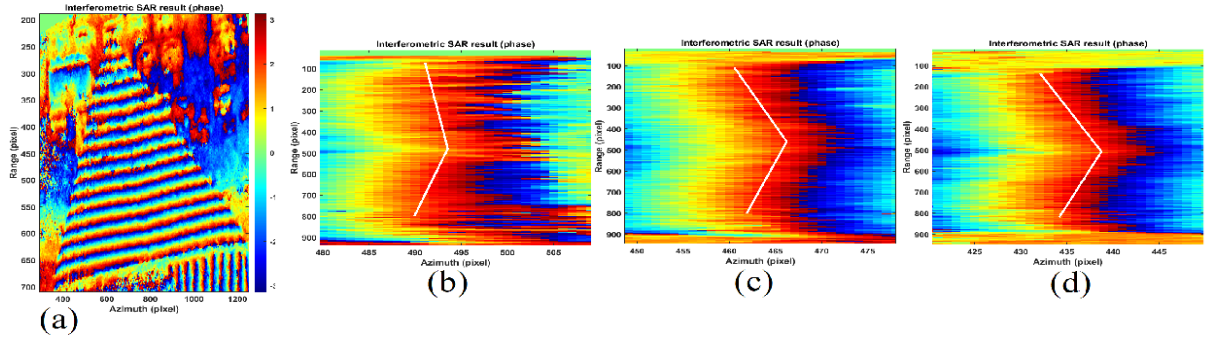

Figure 9. Representation in particular of the pyramid of Khnum-Khufu. Interferometric fringes. (a): North side. (b,c,d): magnification of interferometric fringe 1,2, and 3.

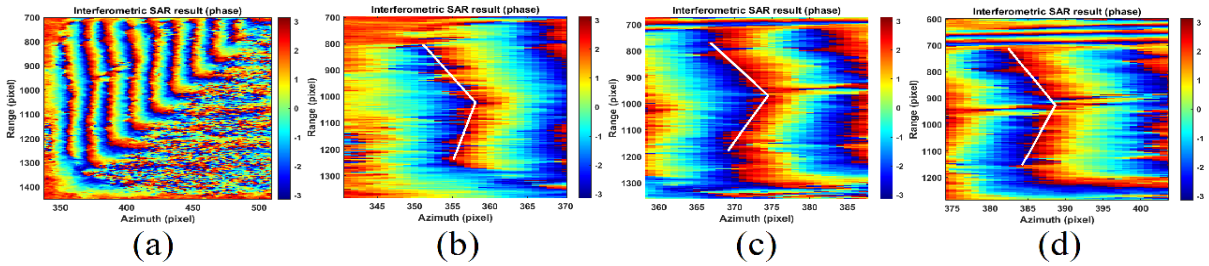

Figure 10. Representation in particular of the pyramid of Khnum-Khufu. Interferometric fringes. (a): East side. (b,c,d): magnification of interferometric fringe 1,2, and 3.

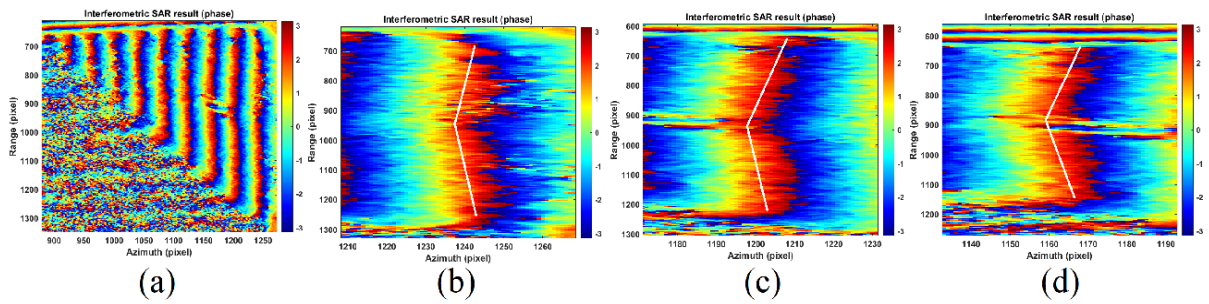

Figure 11. Representation in particular of the pyramid of Khnum-Khufu. Interferometric fringes. (a): West side. (b,c,d): magnification of interferometric fringe 1,2, and 3.

Preprints (www.preprints.org) | NOT PEER-REVIEWED | Posted: 18 August 2022 doi:10.20944/preprints202208.0329.v1

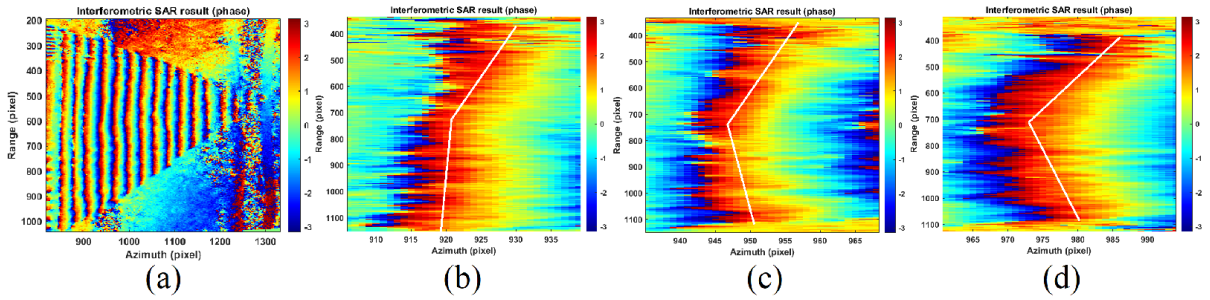

Figure 12. Representation in particular of the pyramid of Kefren. Interferometric fringes. (a): North side. (b,c,d): magnification of interferometric fringe 1,2, and 3.

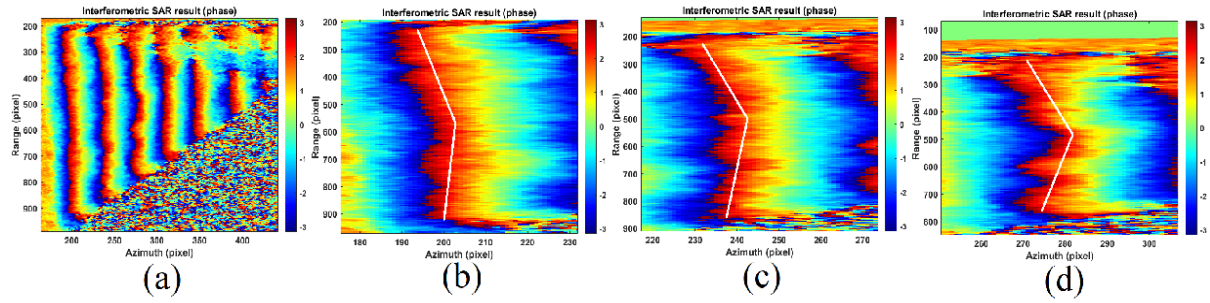

Figure 13. Representation in particular of the pyramid of Kefren. Interferometric phases. (a): Est side. (b,c,d): magnification of interferometric fringe 1,2, and 3.

detailed explanation is provided in the subsection 6. Similarly the results for the internal vibrational tomography analysis of Khnum-Khufu alone, are discussed in detail in subsection 7.

6. External Measurements

This subsection shows and discusses all the results obtained with the aim of revealing new features of the external appearance of all pyramids residing on the Giza Plateau. In order to achieve this goal, we employed the InSAR technique and evaluated the nature of the interferometric fringes and discovered, through the measurement of their inclination, that all pyramids do not each consist of four faces but of eight faces. We found that each face of each pyramid had an inwards bow that became more relevant closer to the ground much like a trough. Figures 6 show the interferometric fringes generated by two SAR repeat-pass acquisitions, with a suitable spatial baseline in order to generate a series of well-estimated interferometric fringes imprinted on the faces of the pyramids. The interferometric acquisition was performed along a time baseline equal to the complete orbital cycle of the single CSG satellite, which coincides with 16 days. In spite of the substantial number of waiting days, the interferometric acquisition appears not to be very noisy and this quality is confirmed through the evaluation of the coherence parameter whose map is represented in Figure 7. This result appears very good, as a large part of the figure, removing all the areas where the radar shadow is present, maintains coherence levels very close to 1.

The Figure 8 (a) represent the details of the InSAR fringes measured on the three pyramids (Khufu, Kefren, and Menkaure), while Figure 8 (b) is the detail of the pyramid of Khnum-Khufu, and finally Figure 8 (c) is the pyramid of Kefren. Figure 9 (a), (b), (c) and (d), are the particular representations of the SAR interferometric fringes observed on the North face of the Pyramid of Khnum-Khufu (in box (a)). The remaining boxes (b), (c) and (d), represent the first, second and third interferometric fringes observed on the North face of the same pyramid, starting from the bottom. The inclination of the entire face of the pyramid is clearly observed, having symmetry along the height of the geometric figure. The east face of the Khnum-Khufu pyramid is depicted in Figure 10 (a), while the details of the first, second and third fringe (starting from the ground plane) are shown in Figure 10 (b), (c) and

Preprints (www.preprints.org) | NOT PEER-REVIEWED | Posted: 18 August 2022 doi:10.20944/preprints202208.0329.v1

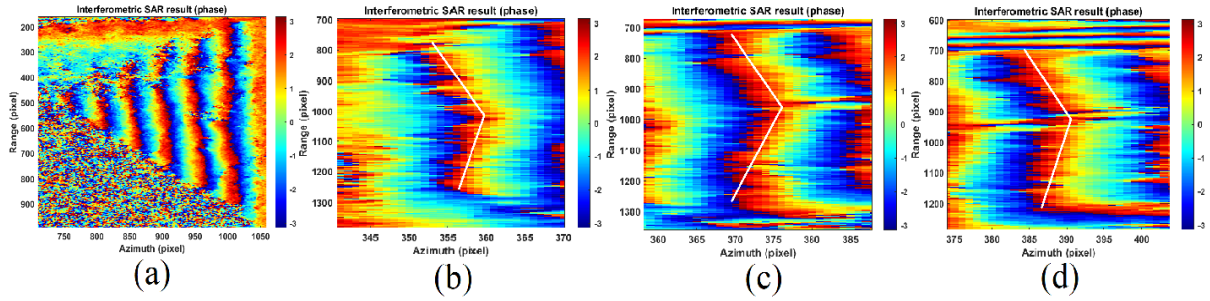

Figure 14. Representation in particular of the pyramid of Kefren. Interferometric phases. (a): West side. (b,c,d): magnification of interferometric fringe 1,2, and 3.

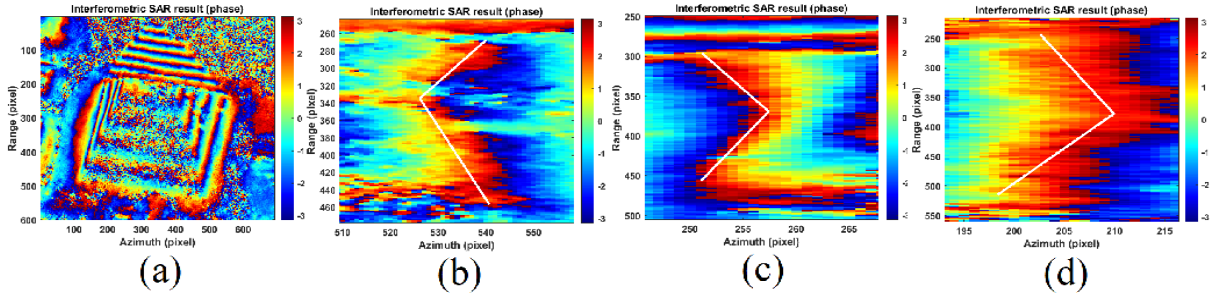

Figure 15. Representation in particular of the pyramid of Menkaure. Interferometric phases. (a): Menkaure pyramid. (b): East-side interferometric fringe particular. (c): West-side interferometric fringe particular. (d): North-side interferometric fringe particular.

(d) respectively. Here again, the same effect is observed whereby the single face is divided into two indented half-faces. The West face also presents the same architectural feature, in fact, Figure 11 (a), depicts the extension of the interferometric fringes extended over the entire West face, while the details of the first, second and third fringes (always starting from the ground plane), are shown in Figure 11 (b), (c) and (d) respectively.

We now move to the pyramid of Kefren to repeat the same experiments where the same qualitative evaluation of the SAR interferometric fringes present on the three facets of it, except for the South one, will be carried out, reaching the identical conclusions made for the pyramid of Khufu. Figure 12 (a), (b), (c) and (d), are the particular representation of the SAR interferometric fringes observed on the North face of the Pyramid of Kefren (in box (a)). The remaining boxes (b), (c) and (d), represent the first, second and third interferometric fringes observed on the North face of the same pyramid, starting from the bottom. The East Front of the second Kefren pyramid is analyzed in Figure 13 (a), depicting the extent of the interferometric fringes as a whole, while the details of the first, second and third fringes (starting from the ground plane) are shown in Figure 13 (b), (c) and (d) respectively. The West Façade is also studied in Figure 14 (a), along with its first, second and third fringe details (starting from the ground plane), which are shown in Figure 14 (b), (c) and (d) respectively.

Although much smaller, the pyramid of Menkaure is also well represented by the interferometric radar. As a matter of fact, Figures (a), (b), (c) and (d) depict the entire pyramid (in Figures (a)), while Figures (b), (c) and (d) depict the first fringe starting from the ground plane of the East, West, and North faces respectively. Surprisingly, the pyramid of Menkaure also consists of eight facets and not four (while maintaining the fact that the south face could not be observed because in radar shadow). This subsection, which focused on presenting the results of external measurements alone, ends by rigorously demonstrating, through radar measurements, the eight-sided nature of the three pyramids of Khufu, Kefren and Menkaure. In the next subsection, the internal measurements that were made from space will be detailed, in order to carry out for the first time the complete internal mapping of all structures belonging to the pyramid of Khnum-Khufu alone.

Preprints (www.preprints.org) | NOT PEER-REVIEWED | Posted: 18 August 2022 doi:10.20944/preprints202208.0329.v1

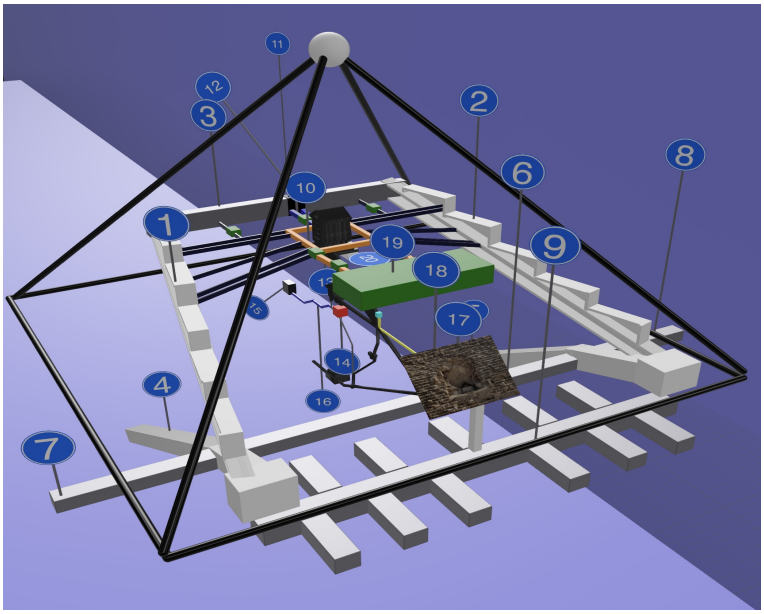

Figure 16. (a): SLC SAR image in magnitude representation of Khnum-Khufu. (b): Schematic representation of Khnum-Khufu.

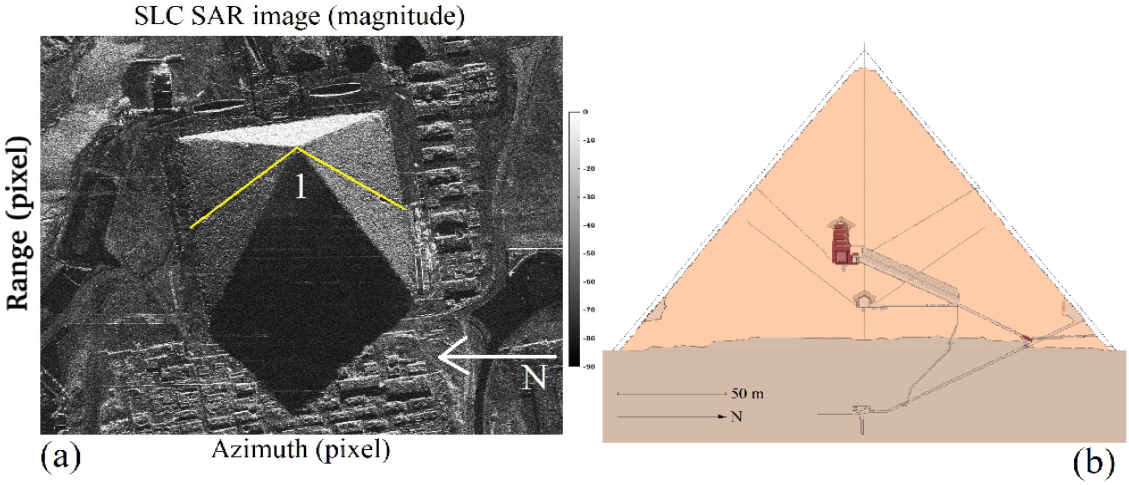

Figure 17. (a): Tomographic map of Khnum-Khufu overlapped to its schematic representation. (b): Tomographic map of Khnum-Khufu.

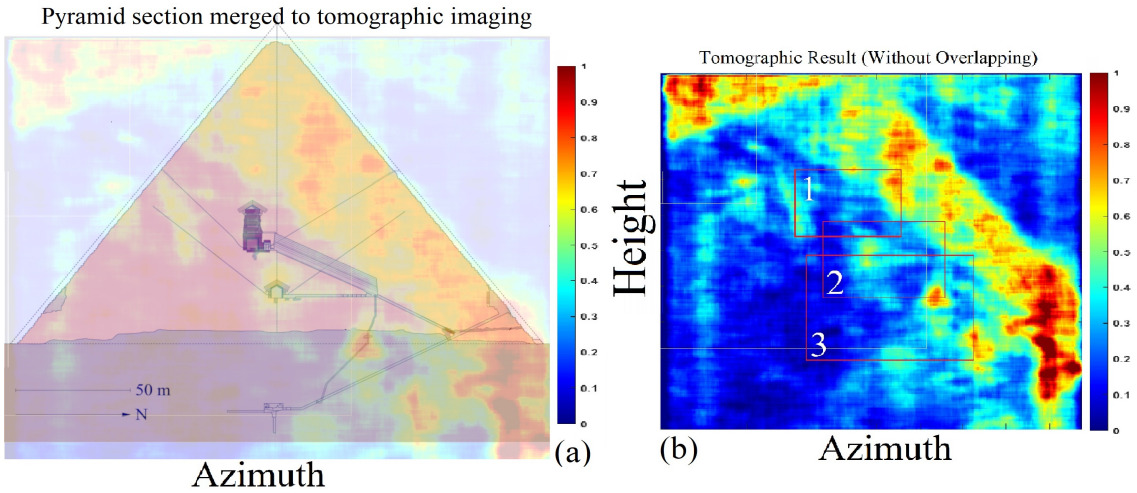

Figure 18. Schematic representation of the Khufu pyramid.

Preprints (www.preprints.org) | NOT PEER-REVIEWED | Posted: 18 August 2022 doi:10.20944/preprints202208.0329.v1

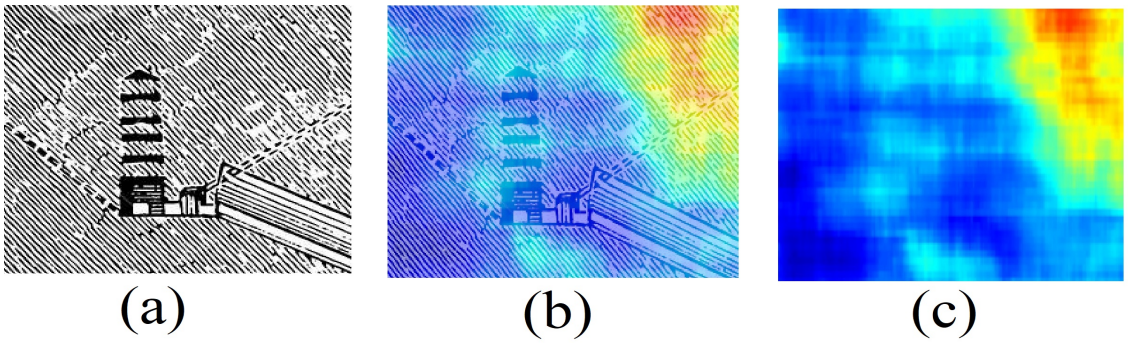

Figure 19. Imagine SAR of the pyramid of Khnum-Khufu. The V-shaped plot represents the tomographic line for which the vibrations were calculated, so that the inner section of the pyramid can be represented.

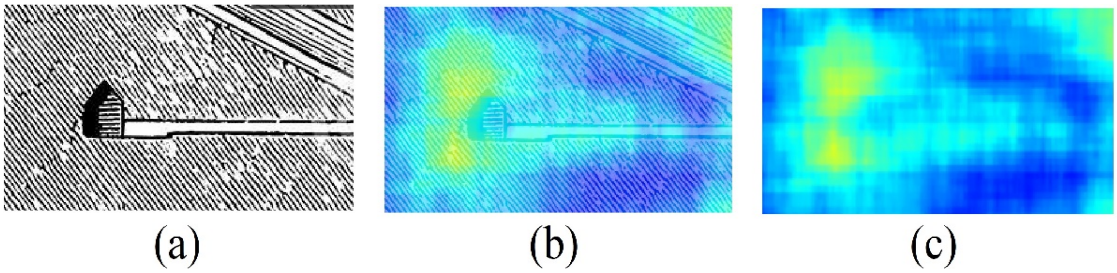

Figure 20. (a): Schematic representation of the ZED (box 1 details of Figure 18 (b)). (b): (b): Schematic representation of the ZED (box 1 details of Figure 18 (b)) partially overlapped to tomographic result. (c): Figure 18 (b) box 1 details Tomographic result.

7. Internal Measurements of Khnum-Khufu

Data analysis obtained using te SAR tomographic Doppler imaging technique was able to provide clear objective elements to understand the internal structure of the pyramid of Khnum-Khufu. When proposing our results, we start by describing the well-known structures and then move on to the description of all the unknown structures. The internal imaging obtained from multiple angles, allow us to obtain an accurate 3D model that gave us the possibility, like never before, to take a look inside one of the most important and mysterious megalithic monuments in the world. This subsection describes all the tomographic measurements and the entire internal architecture of Khnum-Khufu has been redesigned, which we propose in Figure 16. The complete list of rooms, corridors and tunnels that had never been inventoried until now is shown in Tab. 3. Each structure (simple or complex) was assigned to a unique tag numbered from 1 to 20, according to Figure 16. For this work, we have not used any kind of simulated data or predictive mathematical model, but rather we report in a scientific manner what the CSG satellite has brought to our attention. Here we list the explanation of all the results obtained respecting the order given in Tab. 3. Each structure listed in Tab. 3 will be described in detail, identified in the tomography and reconstructed within a Computer-Aided Design and Drafting (CAD) environment where all measurements will be provided.

7.1. Imaging of known structures

Before describing what has been discovered (what is still unknown) we propose the imaging of the known objects, in particular the King's room, the Zed, the Queen's room, the Grand Gallery, the grotto, and the so-called unfinished room. The SAR image of the pyramid is shown in Figure 17 (a), while the internal diagram of the pyramid, oriented towards the North (the Northern direction goes from left to right) is shown in Figure 17 (b). The first tomographic result is presented in Figure 18 (a) and (b). This result is illustrated in Figure 17 (a) by means of two yellow lines (identified by the number 1) that extend from the ground towards the pyramid apex. By estimating the vibrations,

Preprints (www.preprints.org) | NOT PEER-REVIEWED | Posted: 18 August 2022 doi:10.20944/preprints202208.0329.v1

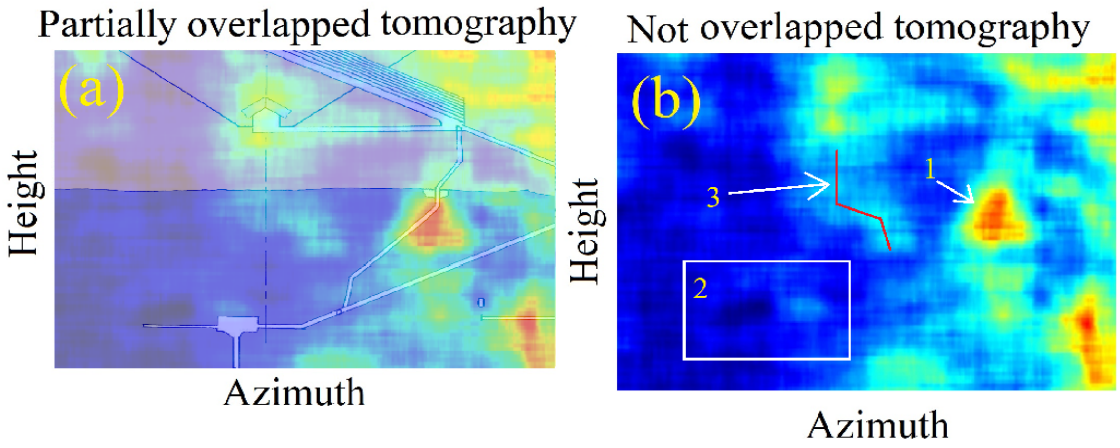

Figure 21. (a): Schematic representation of Figure 18 (b) box 3 details partially overlapped with tomographic result. (b): tomographic result of Figure 18 (b) box 3 details.

the pyramid is transparent like a crystal due to their penetration characteristics within the solid rock, and its internal structures can be observed in Figure 18 (a) and (b). Figure 18 (a) represents the sonic tomography partially overlapped with the picture in Figure 17 (b), while Figure 17 (b) shows the non-overlapped tomography where three areas of interest are shown, and details are below studied. Figure 19 (a), (b) and (c) is the detailed representation of the ZED, located inside box number 1 of Figure 18(b), where 19 (a) is the schematic representation, while Figures 19 (b) and (c) are the partially overlapped, and not-overlapped tomography magnitude images respectively. The Queen's chamber particular is depicted in Figure 20 (a), (b) and (c), here we use the same representation strategy where 20 (a) is the room scheme and Figures 20 (b) and (c) are the partially overlapped and not-overlapped tomography respectively. Figure 21 (a) and (b) is the detailed image contained within the red box 3 of Figure 18 (b) and the void commonly referred to as 'the Grotto' is clearly visible. The lower chamber, the one commonly referred to as 'the unfinished room', is detected by radar, although with a weak signal, within the white box number 2. The Queen's room appears to be connected through a corridor connecting the grotto to the room below. This corridor, although it appears to be abruptly interrupted, is detected through a radar signature, which is marked by the white arrow number 3. It is assumed that this corridor follows the trajectory indicated by the red line, also pointed out by the white arrow number 3. Figure 2 (b) and (c) show the detailed figure of the ZED, the colossal monument located at the heart of the pyramid (visible in Figure 18 (a)). Figure 2 (b) is its representation along the West-East direction, while Figure 2 (c) shows its pattern along the South-North direction. Concluding this section we propose in Figure 22 (a) and (b) the partially and not-overlapped tomography of the Zed respectively, where also the King's chamber is visible.

Here we show in sequence all the tomographies we have calculated, whereby for each of them the subpicture (a) represents the SAR image in magnitude, whereby the tomographic line of investigation is visible (indicated with a yellow line marked with the number 1), while subpicture (b) represents the tomogram (again in magnitude). In order to be more clear, we report the aforementioned figures in Table 2:

7.2. Eastern and Western ascending ramps (tag 1, tag 2)

Two inclined and diverging ramps (identified with the numbers 1 and 2 in the 3D reconstruction depicted in Figure 16), characterized by an approximate slope of about 42 degrees, located inside the West and East sides. For both ramps, the lower part starts from the ground level on the North side and reaches half the height of the pyramid on the south side. The reference images are Figure 34 (a), (b), for the Eastern side, and Figure 35 (a), (b), for the Western side, where the 3D models are compared to measured tomograms. From the figures, tags number 1,2,3,4 5,7 and 9 are recognized.

Preprints (www.preprints.org) | NOT PEER-REVIEWED | Posted: 18 August 2022 doi:10.20944/preprints202208.0329.v1

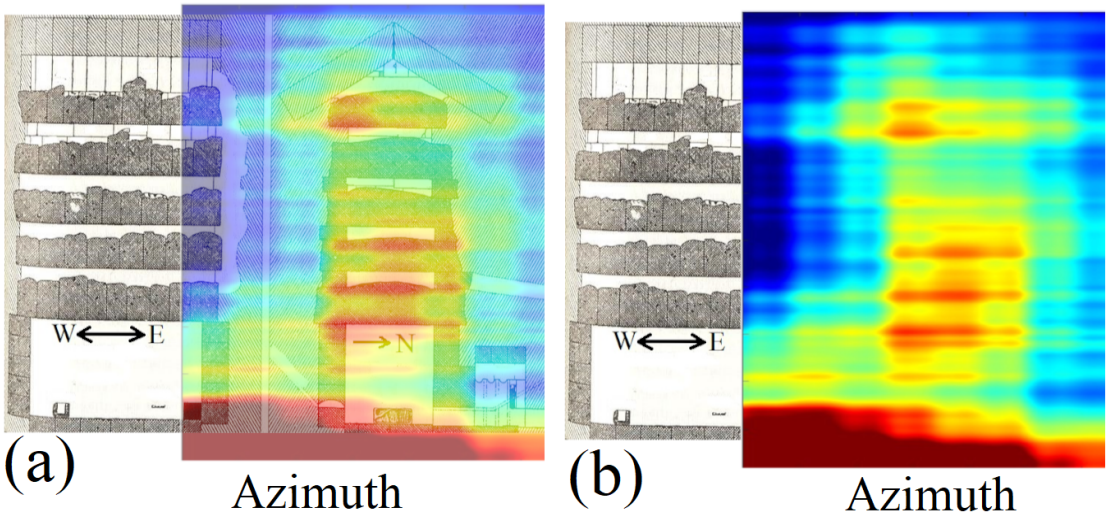

Figure 22. Schematic representation of the King chamber and the Zed.

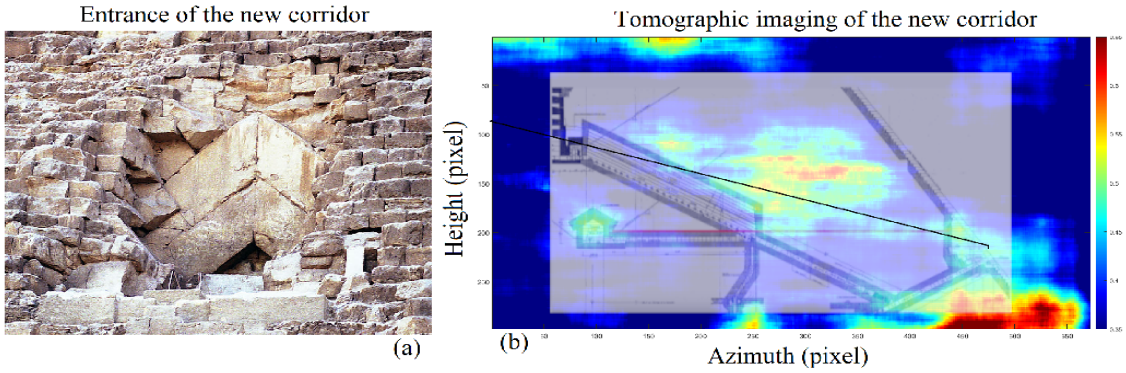

Figure 23. Entrance on Khnum-Khufu. (a): Optical image. (b): Tomographic map (magnitude).

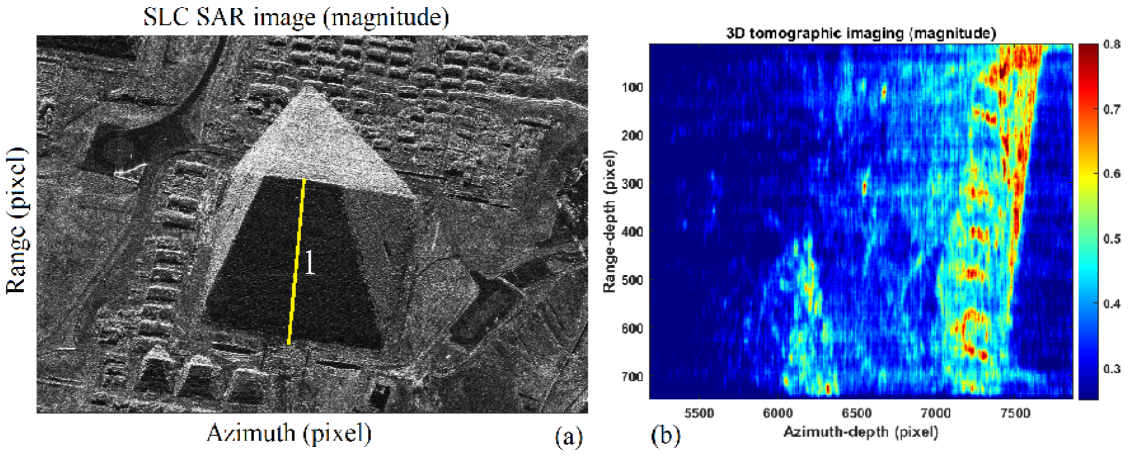

Figure 24. SAR images. (a): SLC SAR image (magnetude). (b): Tomography.

Preprints (www.preprints.org) | NOT PEER-REVIEWED | Posted: 18 August 2022 doi:10.20944/preprints202208.0329.v1

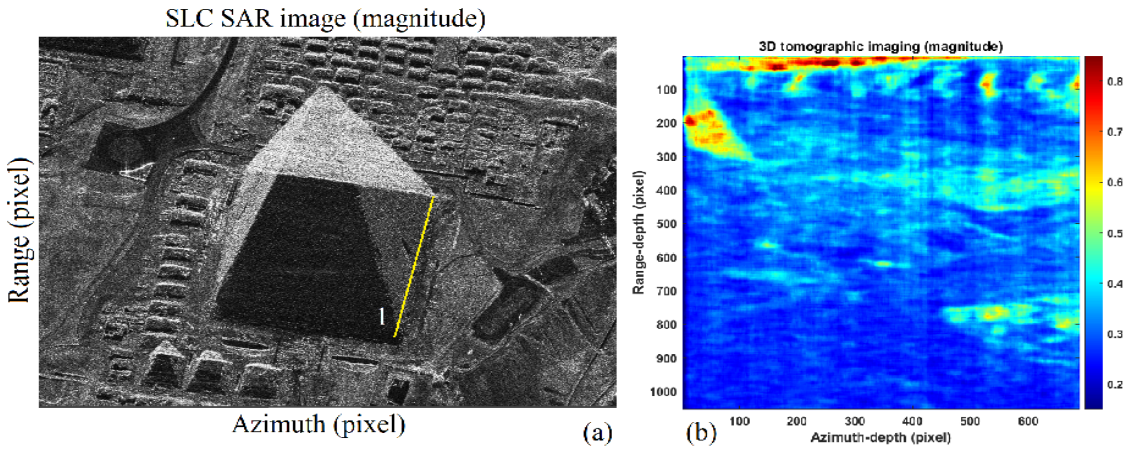

Figure 25. SAR images. (a): SLC SAR image (magnetude). (b): Tomography.

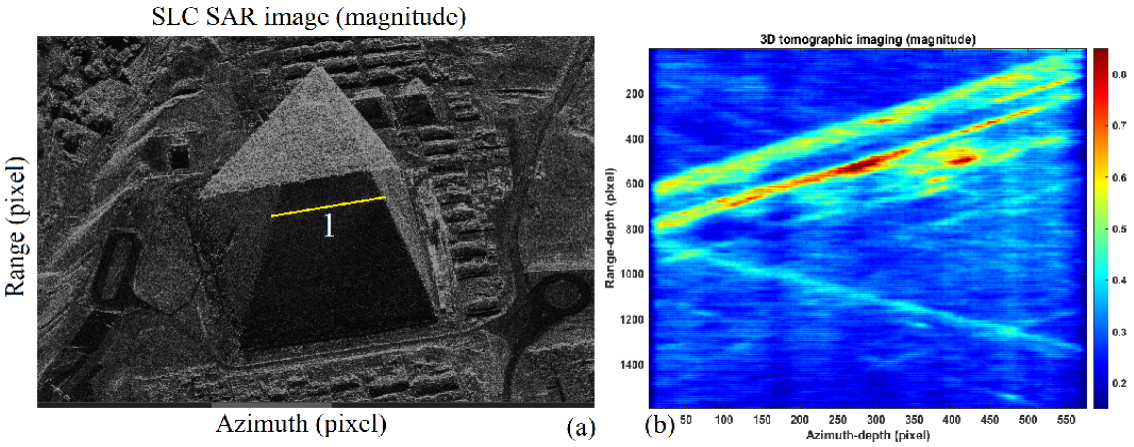

Figure 26. SAR images. (a): SLC SAR image (magnetude). (b): Tomography.

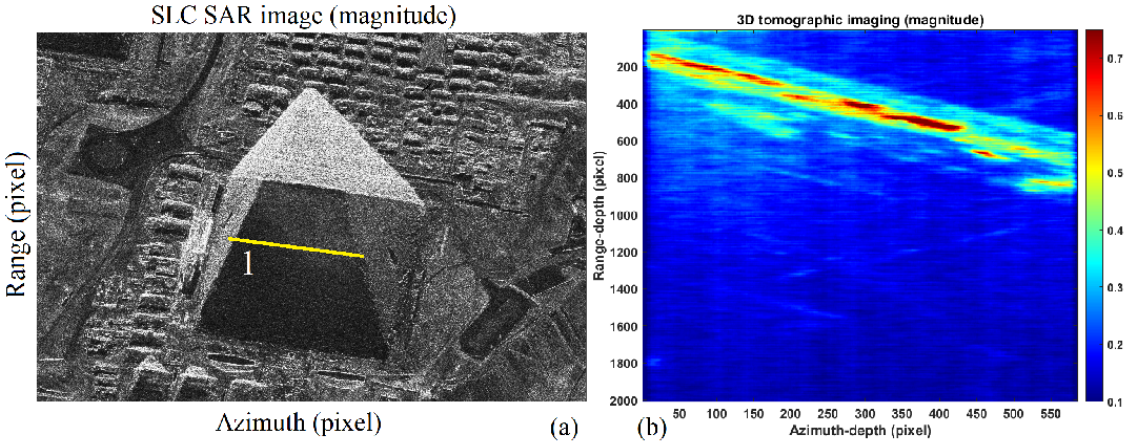

Figure 27. SAR images. (a): SLC SAR image (magnetude). (b): Tomography.

Preprints (www.preprints.org) | NOT PEER-REVIEWED | Posted: 18 August 2022 doi:10.20944/preprints202208.0329.v1

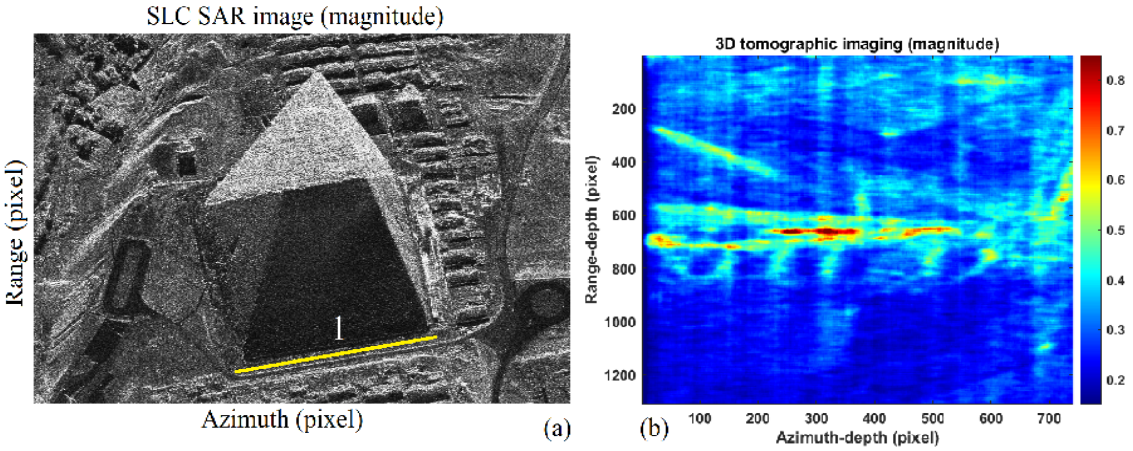

Figure 28. SAR images. (a): SLC SAR image (magnetude). (b): Tomography.

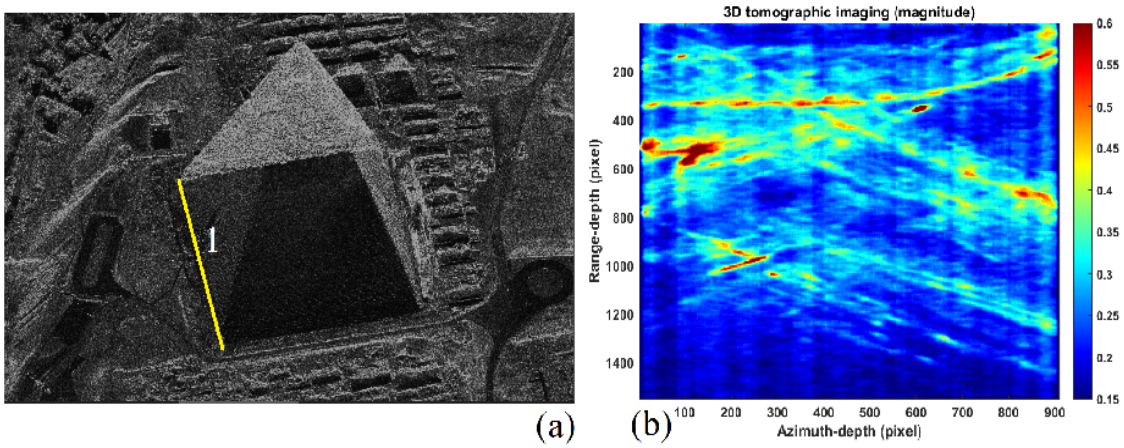

Figure 29. SAR images. (a): SLC SAR image (magnetude). (b): Tomography.

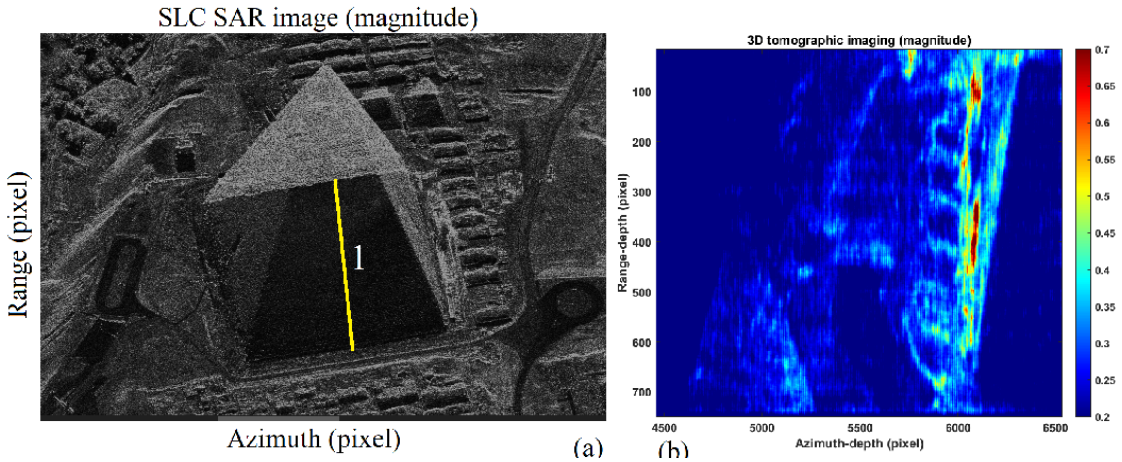

Figure 30. SAR images. (a): SLC SAR image (magnetude). (b): Tomography.

Preprints (www.preprints.org) | NOT PEER-REVIEWED | Posted: 18 August 2022 doi:10.20944/preprints202208.0329.v1

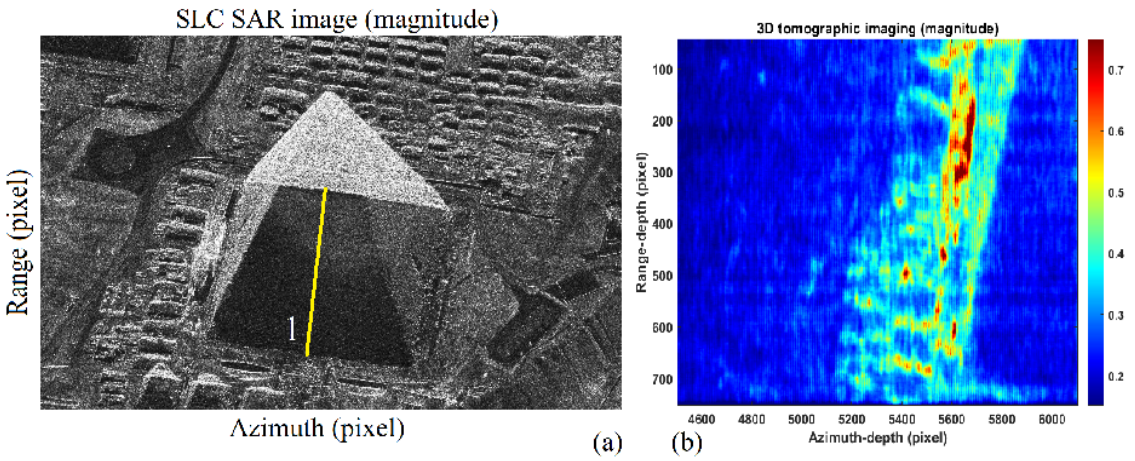

Figure 31. SAR images. (a): SLC SAR image (magnetude). (b): Tomography.

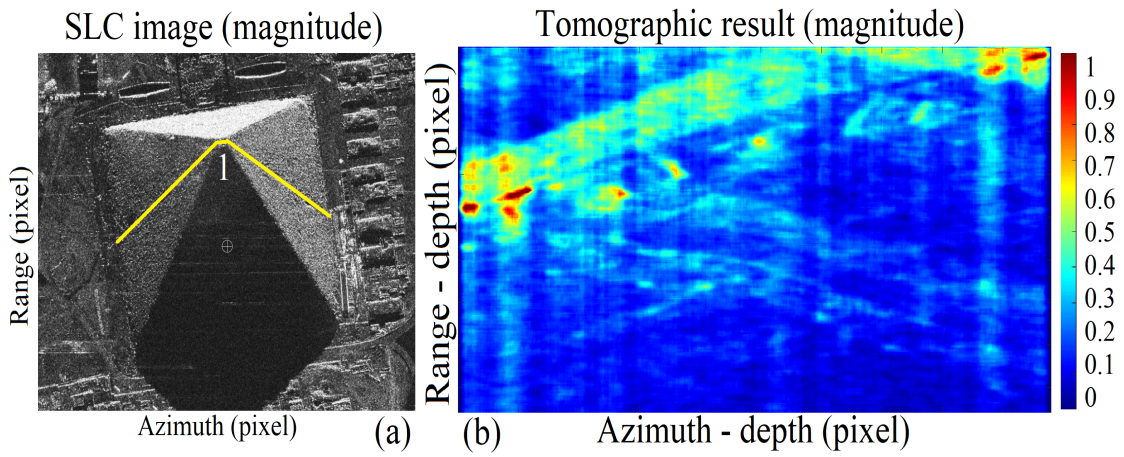

Figure 32. SAR images. (a): SLC SAR image (magnetude). (b): Tomography.

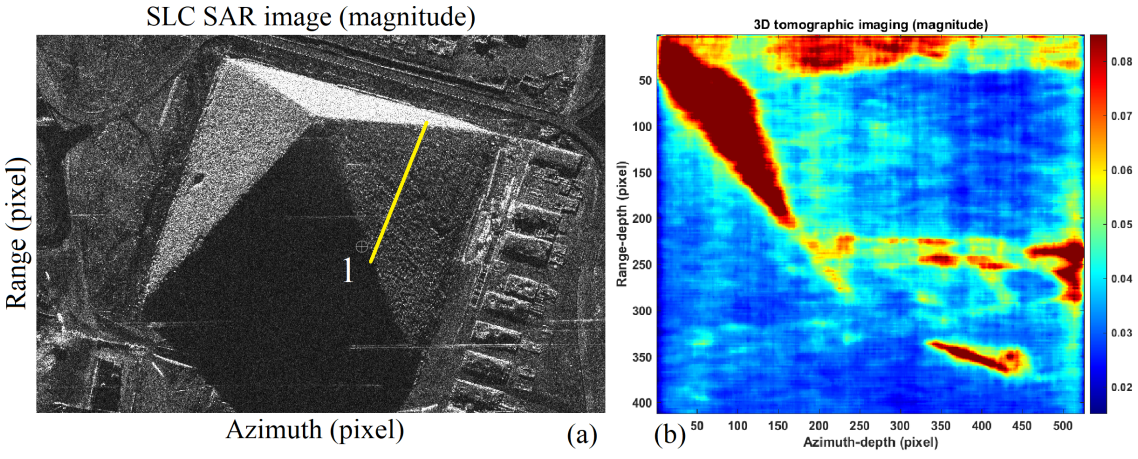

Figure 33. SAR images. (a): SLC SAR image (magnetude). (b): Tomography.

Preprints (www.preprints.org) | NOT PEER-REVIEWED | Posted: 18 August 2022 doi:10.20944/preprints202208.0329.v1

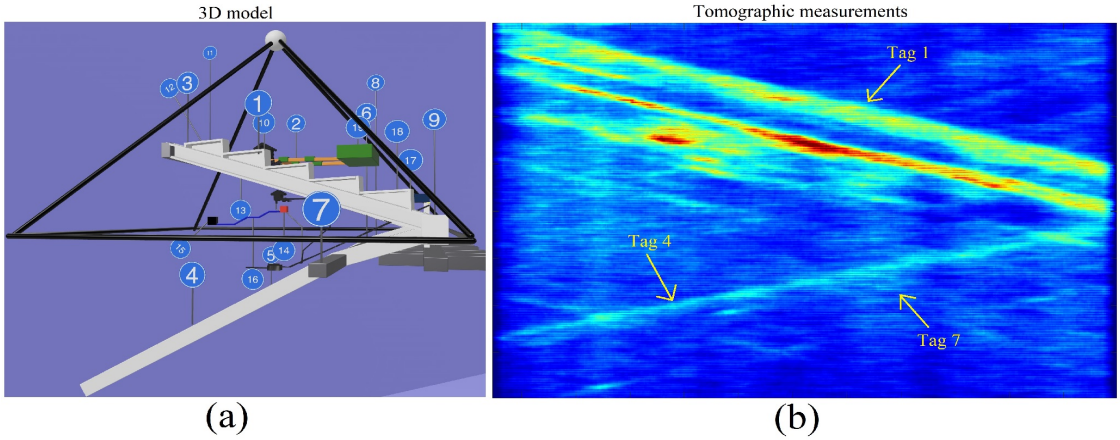

Figure 34. Tags association from tomography to 3D model. (a): 3D model of Khnum-Khufu. (b): Tomography.

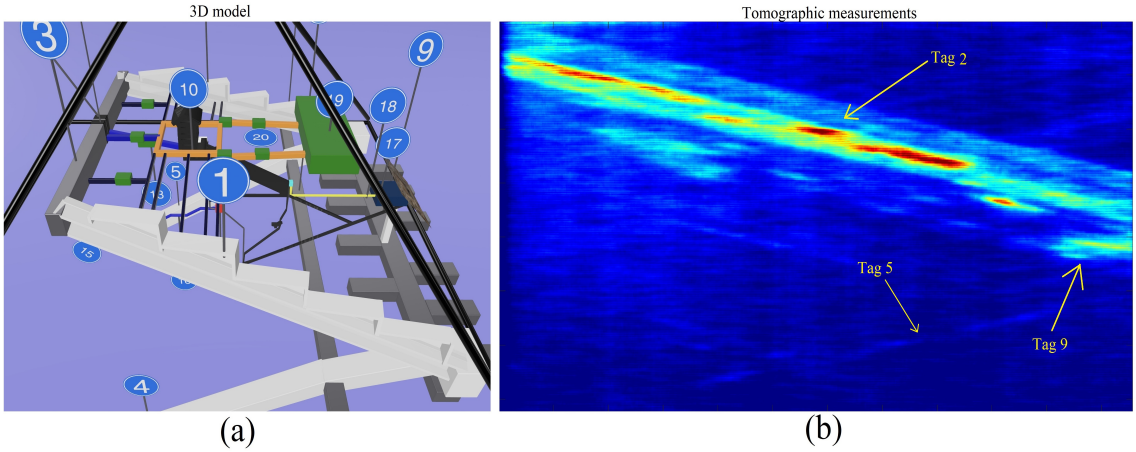

Figure 35. Tags association from tomography to 3D model. (a): 3D model of Khnum-Khufu. (b): Tomography.

Preprints (www.preprints.org) | NOT PEER-REVIEWED | Posted: 18 August 2022 doi:10.20944/preprints202208.0329.v1

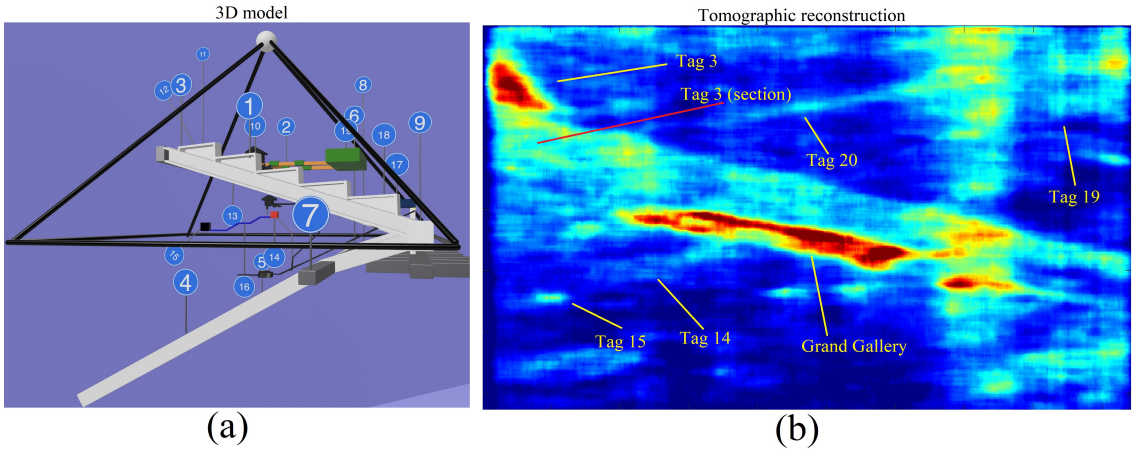

Figure 36. Tags association from tomography to 3D model. (a): 3D model of Khnum-Khufu. (b): Tomography.

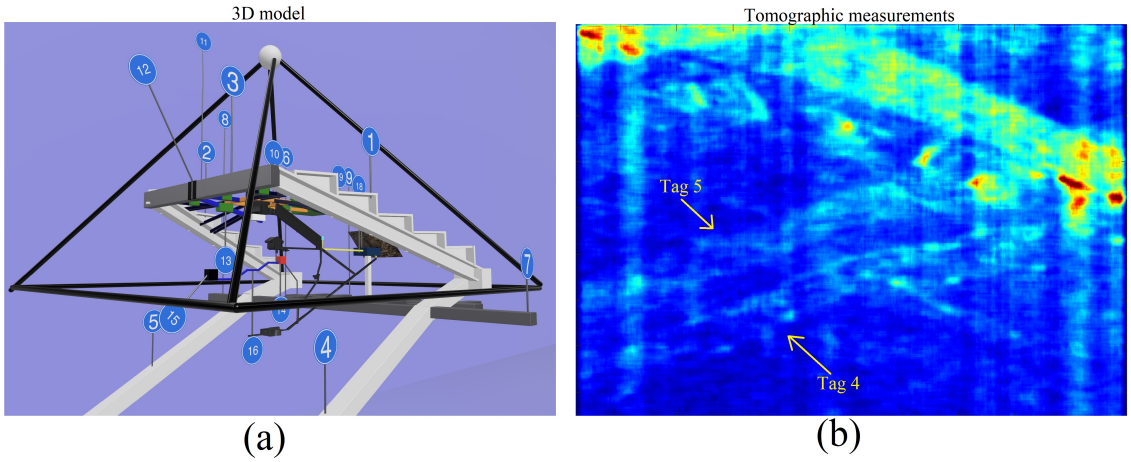

Figure 37. Tags association from tomography to 3D model. (a): 3D model of Khnum-Khufu. (b): Tomography.

7.3. Southern Corridor, (tag 3)

The ascending corridors are connected to each other by means of a horizontal structure placed at a height of about 90 meters and located near the south side of the pyramid (identified with the number 3 in Figure 16). The corridor is recognized in Figure 36 (b), where the 3D reconstruction can be seen in Figure 36 (b).

7.4. Eastern and Western descending ramps, (tag 4, tag 5)

Two ramps that, both connected to the previous ones, parallel to each other and also to the East and West base sides that run through a descending underground section with variable slope (numbers 4 and 5 in the 3D model). Figures 37 (a) and 38 (a) are the 3D reconstruction models showing the descending corridors from two different view angles, while Figures 37 (b) and 38 (b) corresponds to tomographic measurements of the same tags, corresponding to the same descending corridors.

7.5. Northern underground corridor, (tag 6) and Northern-East and Northern-West underground corridors (tag 7, tag 8)

At the point where descending ramps (tags 4 and 5) increase slope they appear connected with the Northern underground corridor (tag number 6 structure), parallel to the North side of the pyramid. The Northern underground corridor is characterized by two extrusions, which are still

Preprints (www.preprints.org) | NOT PEER-REVIEWED | Posted: 18 August 2022 doi:10.20944/preprints202208.0329.v1

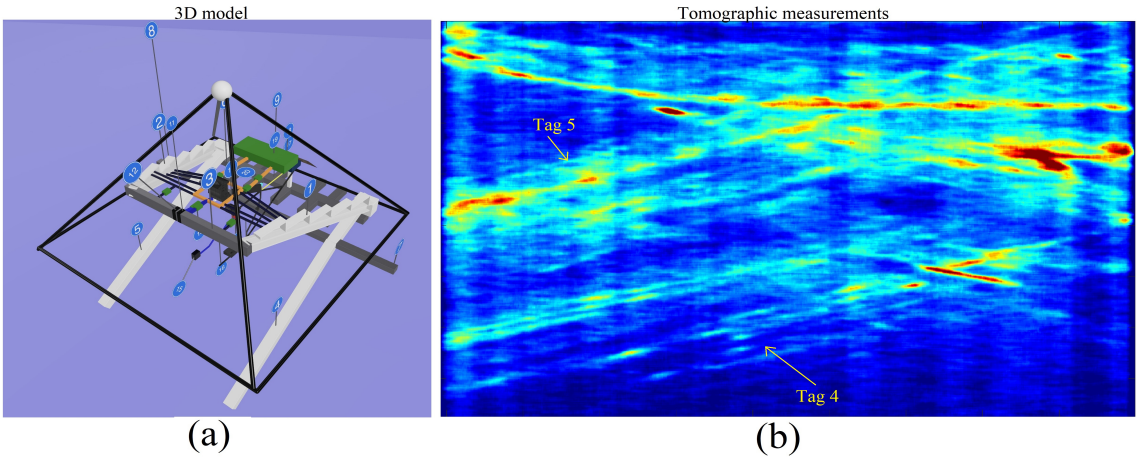

Figure 38. Tags association from tomography to 3D model. (a): 3D model of Khnum-Khufu. (b): Tomography.

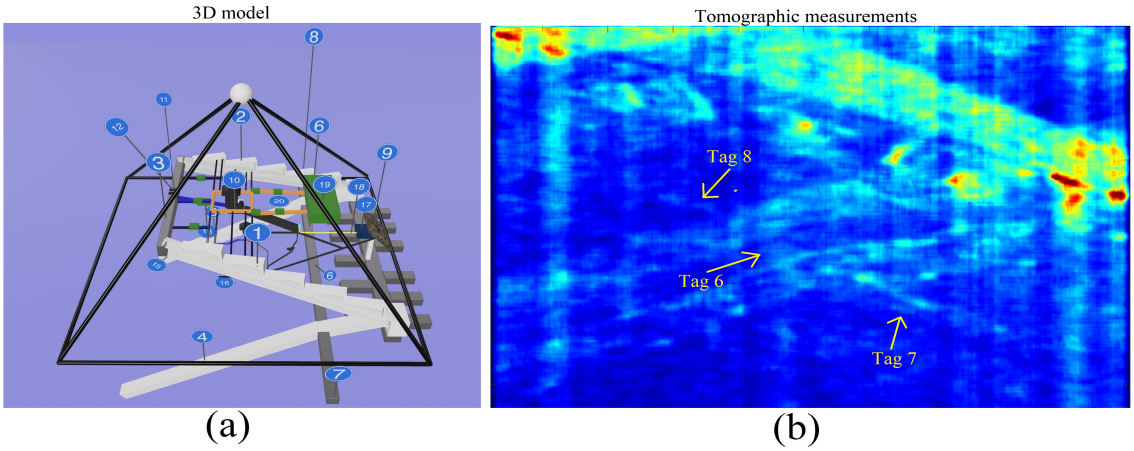

Figure 39. Tags association from tomography to 3D model. (a): 3D model of Khnum-Khufu. (b): Tomography.

located underground. Figure 39 (a) is the 3D reconstruction model showing the structures tagged by numbers 6, 7 and 8, while 39 (b) corresponds to tomographic measurements of the same tags, corresponding to the same descending corridors. The section of this structure is deducted on the tomogram of Figure 40 (b), while the corresponding 3D model is showed in Figure 40 (a).

7.6. Northern underground complex-structure (tag 9)

Immediately below the base of the pyramid structure, at the North side, a complex structure appears consisting of a horizontal body from which several identical bodies branch off, extruded perpendicularly to the main structure and characterized by a geometry, also present in other Egyptian pyramids, such as the pyramid of Zawyet El-Aryan [6,7,59] and the Sekhemkhet pyramid [60] . This complex structure (Number 9 in the 3D model) is characterized by a small conduit placed in a central position that runs a short distance in a vertical direction, in analogy with the presence of a similar building also in El-Aryan [6,7,59] and Saqqara [60]. The reference tomography is shown in Figure 42 (b), while the 3D model is depicted in Figure 42 (a).

7.7. ZED complex-structure (tag 10)

A complex square structure (identified with the number 10 tag), which connects itself to the structure number 11, belonging to the structure of passage number 3. The structure 10 develops around the Zed, approximately at the height of the lowest room (Davison's Chamber) [13]. The

Preprints (www.preprints.org) | NOT PEER-REVIEWED | Posted: 18 August 2022 doi:10.20944/preprints202208.0329.v1

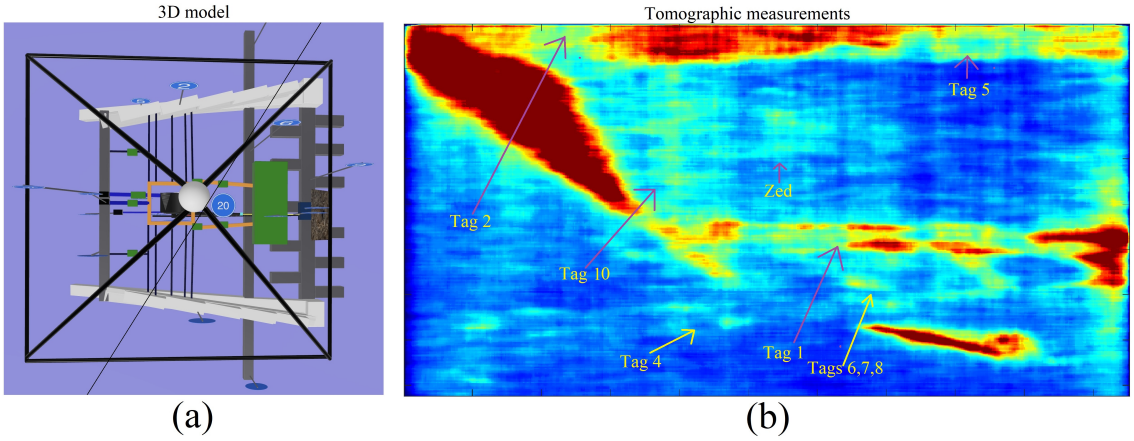

Figure 40. Tags association from tomography to 3D model. (a): 3D model of Khnum-Khufu. (b): Tomography.

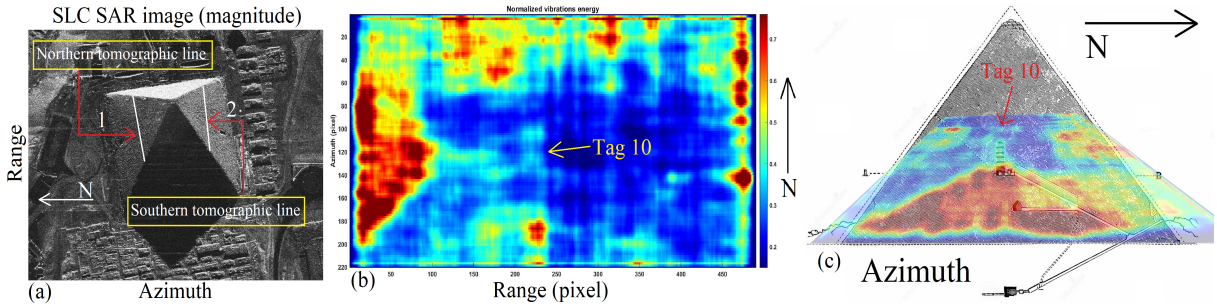

Figure 41. SLC SAR image (magnitude).

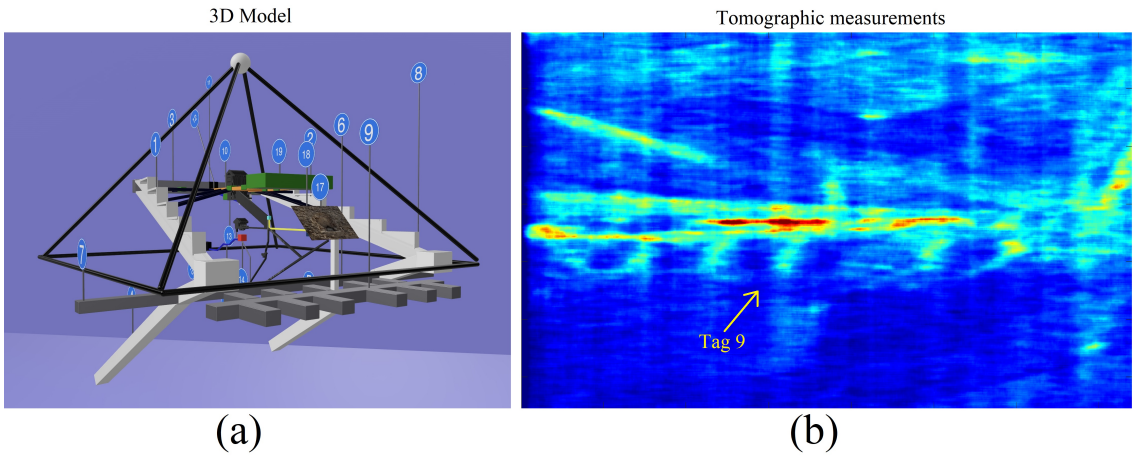

Figure 42. Tags association from tomography to 3D model. (a): 3D model of Khnum-Khufu. (b): Tomography.

Preprints (www.preprints.org) | NOT PEER-REVIEWED | Posted: 18 August 2022 doi:10.20944/preprints202208.0329.v1

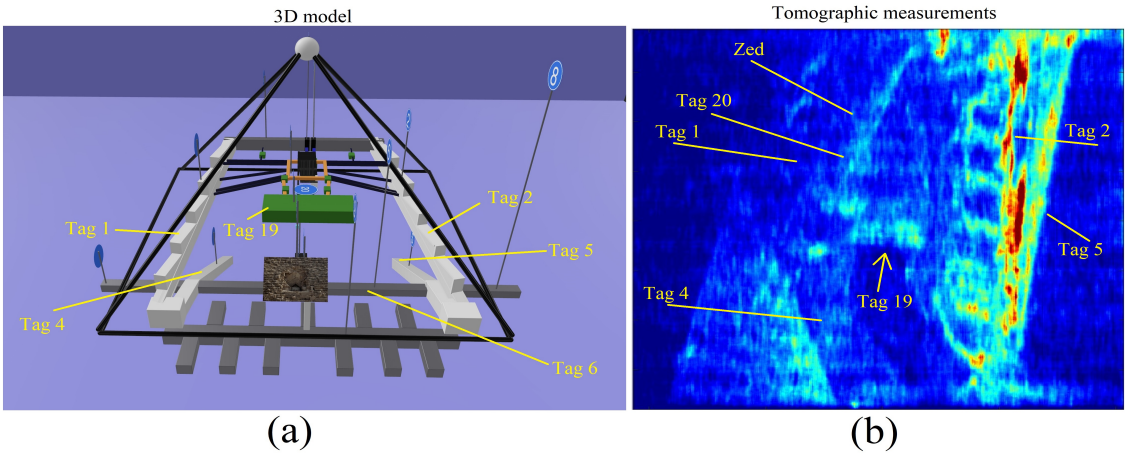

Figure 43. Tags association from tomography to 3D model. (a): 3D model of Khnum-Khufu. (b): Tomography.

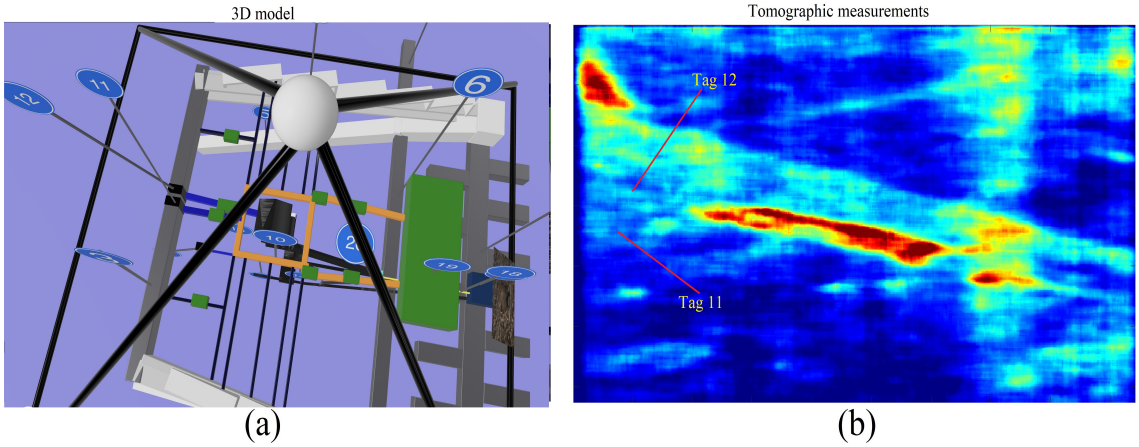

Figure 44. Tags association from tomography to 3D model. (a): 3D model of Khnum-Khufu. (b): Tomography.

reference tomography is shown in Figure 40 (b), while the 3D model is depicted in Figure 40 (a). The structure is also detected through different tomograms depicted in Figure 41 (b), (c), where the reference SLC image is showed in Figure 41 (a), and the tomographic lines 1 and 2 are showed on the northern and southern pyramid surfaces respectively.

7.8. Eastern and western sarcophagus passages facility (tag 11 and tag 12)

Structure number 3 also seems to contain two sub-structures, identified with the numbers 11 and 12, connected, through corridor 13, to the King's room, through a passage that seems located under the floor of the latter. The reference tomography is shown in Figure 44 (b), while the 3D model is depicted in Figure 44 (a).

7.9. Bottom sarcophagus room facility (tag 13)

A room located below structures 11 and 12, connecting facilities 3 to 13. The reference tomography is shown in Figure 45 (b), while the 3D model is depicted in Figure 45 (a). The reference tomography is shown in Figure 47 (b), while the 3D model is depicted in Figure 47 (a).

Preprints (www.preprints.org) | NOT PEER-REVIEWED | Posted: 18 August 2022 doi:10.20944/preprints202208.0329.v1

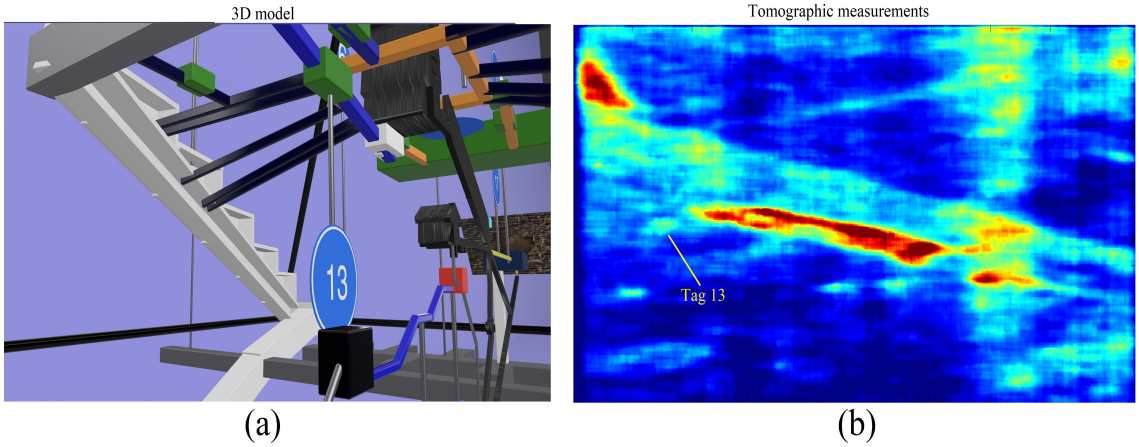

Figure 45. Tags association from tomography to 3D model. (a): 3D model of Khnum-Khufu. (b): Tomography.

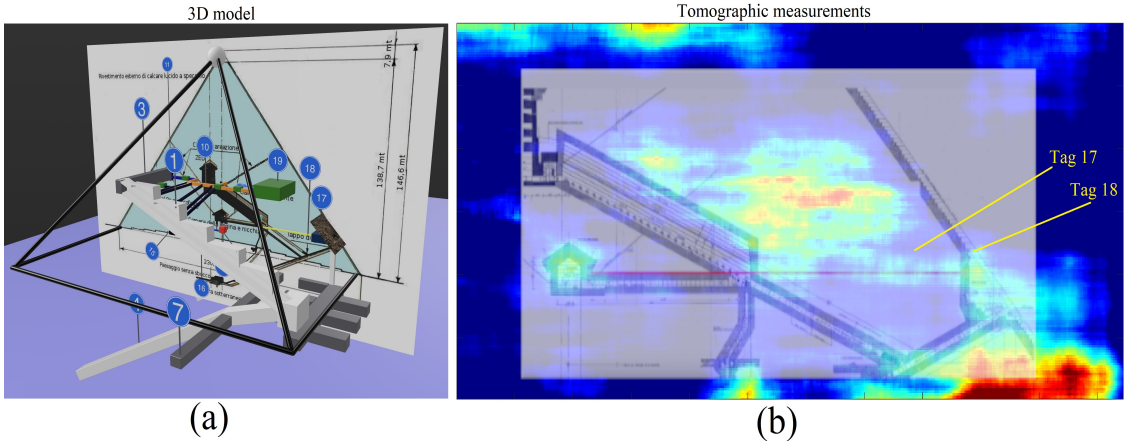

Figure 46. Tags association from tomography to 3D model. (a): 3D model of Khnum-Khufu. (b): Tomography.

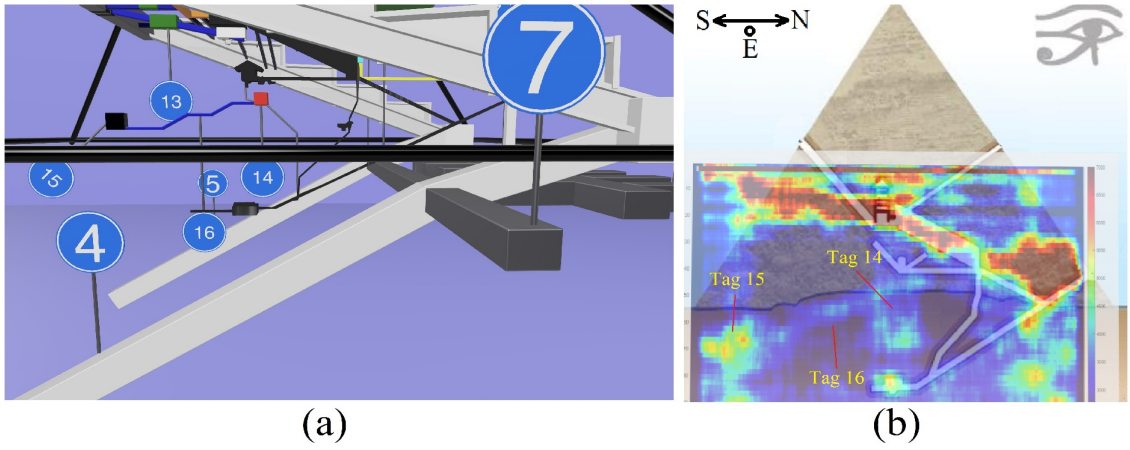

Figure 47. Tags association from tomography to 3D model. (a): 3D model of Khnum-Khufu. (b): Tomography.

Preprints (www.preprints.org) | NOT PEER-REVIEWED | Posted: 18 August 2022 doi:10.20944/preprints202208.0329.v1

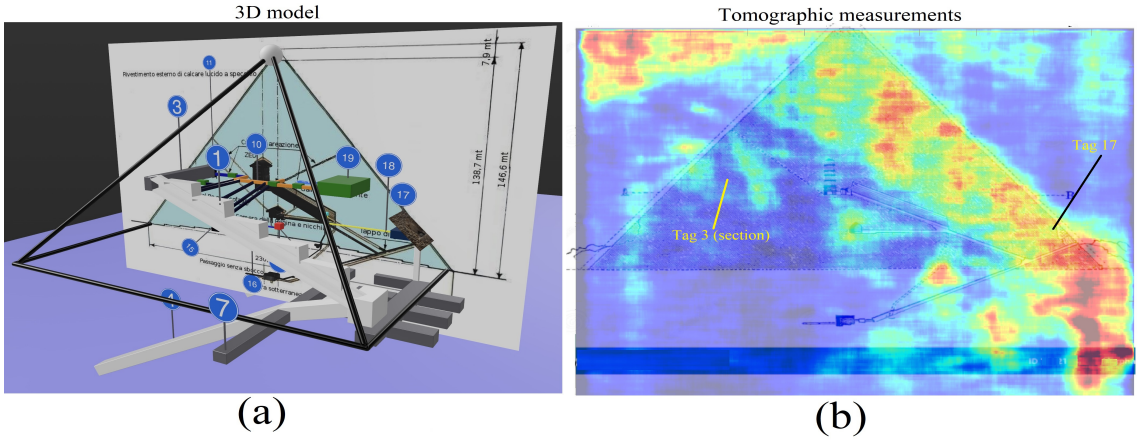

Figure 48. Tags association from tomography to 3D model. (a): 3D model of Khnum-Khufu. (b): Tomography.

7.10. Queen's bottom room (tag 14)

A further structure (identified with the number 14 in the 3D model), located below the Queen's chamber and connected to it through a small conduit. From space number 14 the conduit seems to continue, bonding a similar path which, from the room known as "Grotto", leads to the underground room called unfinished". The reference tomography is shown in Figure 47 (b), while the 3D model is depicted in Figure 47 (a).

7.11. Southern bottom room (tag 15)

A room located on the bottom of structures 11 and 12. The reference tomography is shown in Figure 47 (b), while the 3D model is depicted in Figure 47 (a).

7.12. Southern Connection (tag 16)

A further conduit (number 16 of the 3D model) joins the structure 14 to a structure, placed almost at ground level (number 15 of the 3D model). This facility has been discovered through tomographic result depicted in Figure 47 (b), where a particular of the 3D model is visible in Figure 47 (a).

7.13. Little-void (tag 17)

A void that can be located immediately behind the original entrance of the pyramid, not easily identificable in shape and size (number 17 of the 3D model), from which a horizontal conduit (number 18 of the 3D model) starts and which seems to end at the foot of the Grand Gallery, but not directly connected to it. This is a void located in front of the Northern entrance of the pyramid [40]. The room is clearly visible in Figure 23 (b), precisely located above the corridor identified by the structure with tag 18. It possible to observe the little-void also on Figure 48 (b), there the reference 2D model is reported in Figure 48 (a).

7.14. Front corridor (tag 18)

A corridor-like structure clearly visible in Figure 23 (b) located just behind the external V-shaped structure depicted in Figure 23 (a). The corridor is detected and its tomographic representation il depicted in Figure 23 (b).

7.15. Big-void (tag 19)

A large structure whose shape resembles a parallelepiped (number 19 of the 3D model). This object appears to be connected to structure 10 by means of a double horizontal connection (number 20

Preprints (www.preprints.org) | NOT PEER-REVIEWED | Posted: 18 August 2022 doi:10.20944/preprints202208.0329.v1

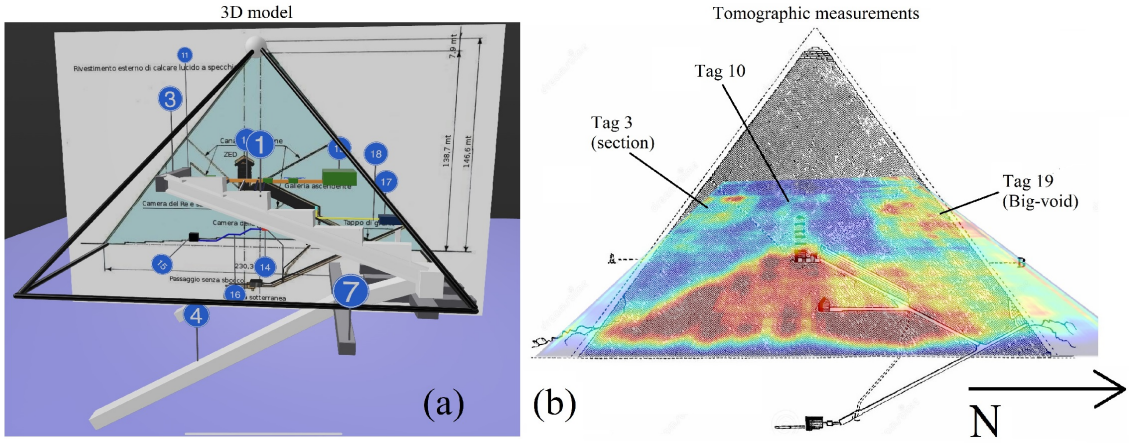

Figure 49. Tags association from tomography to 3D model. (a): 3D model of Khnum-Khufu. (b): Tomography.

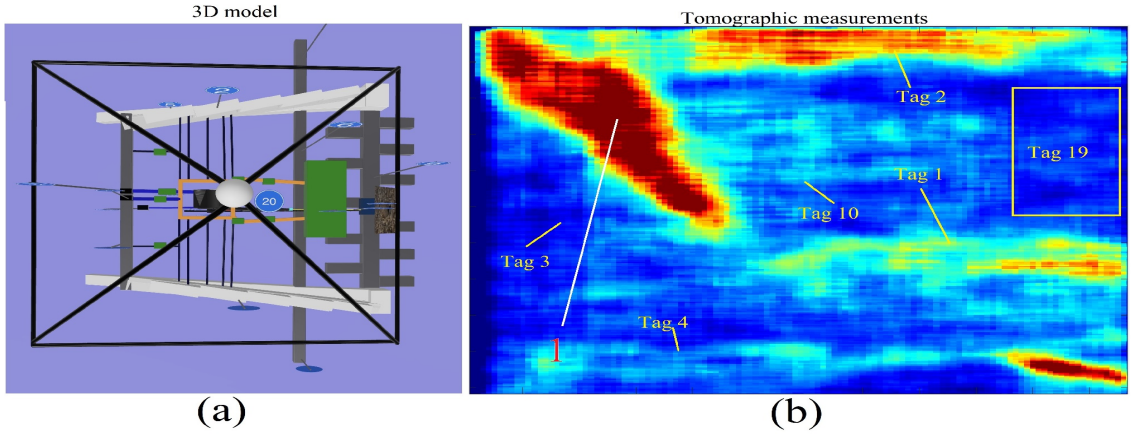

Figure 50. Tags association from tomography to 3D model. (a): 3D model of Khnum-Khufu. (b): Tomography.

of the 3D model). The reference tomography images are shown in Figures 49 (b) 50 (b) and , while the 3D models are depicted in Figure 49 (a) and 50 (a). The large red target 1 visible in Figure 50 (b) is a false alarm, generated by the south-west ascending angle of the pyramid [61].

7.16. ZED-Big-void double connection (tag 20)

Structure 19 (big-void) is connected to the large corridor 3 to the south, at the height of the big-void, via two oblique corridors. The reference tomography is that shown in Figure 36 (b), while the reference 3D model is that in Figure 44 (a).

7.17. Metric determination

The final objective of this study is to provide approximate measurements of the structures detected using the Doppler SAR tomography technique. The measurements that we propose are expressed in metres and are affected by an error that we have estimated to be very low, with respect to the actual measurement of the structures, according to the particular methodology we used. The dimensions are proposed in Figures 51, 52 and 53. The measurements we suggest also include the thickness of the material used to construct them and are not to be intended as mere empty space. With regard to obtaining only empty space, research is currently underway in order to improve the technique and find a way to distinguish solid spaces from hollow spaces. The measures reported are evaluated by using Tape Measuring Wall

Preprints (www.preprints.org) | NOT PEER-REVIEWED | Posted: 18 August 2022 doi:10.20944/preprints202208.0329.v1

Area software (http://www.pictureenginecompany.com/MeasureEngine/Promo.html) emploing as internal standard the pyramid's base lenght and are in accordance whith the results afforded by Sar data.

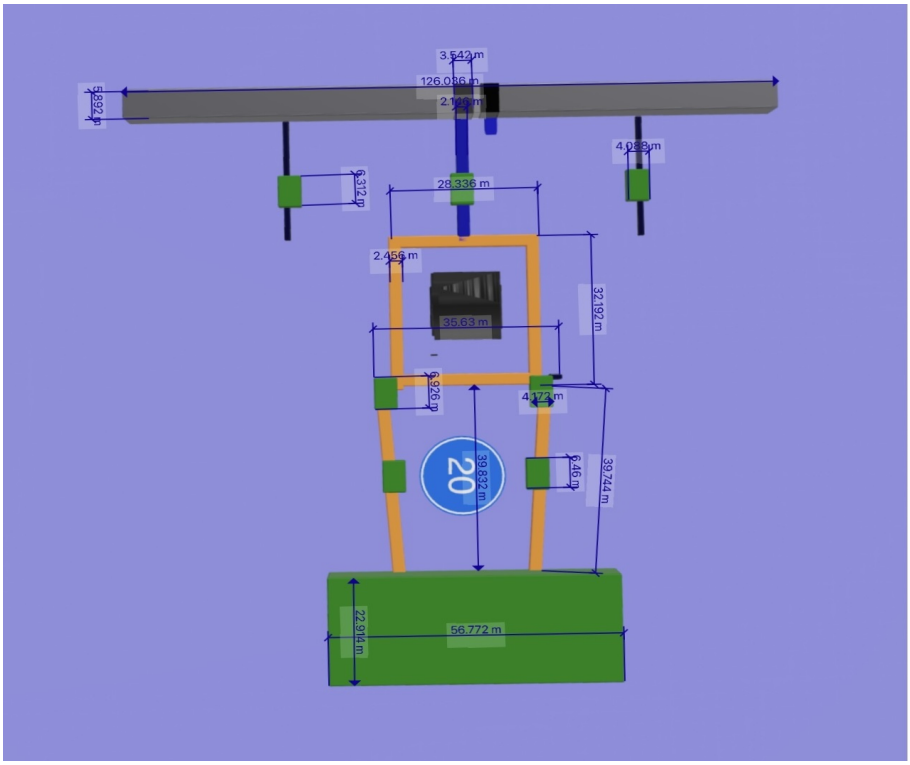

Figure 51. Measurements of the detected facilities of the pyramid. The numbers shown after the comma can not be significant.

8. Discussion

8.1. Data analysis

Here we proceed to data analysis, while being aware that some aspects of the internal structure of the pyramid of Khnum-Khufu still need to be clarified, it is possible, in our opinion, to attribute a meaning to the internal structures of the monument, taking into account all the data relating to previous research in this field. It is possible to underline how our 3D reconstruction, even if for now it does not claim to indicate the true measurements of the objects shown, (even if the SAR technique can accurately evaluate this parameter), is following some facts exposed in previous research. Some researchers have shown how on the North edge of the East side of the pyramid at ground level, there is a thermal anomaly that suggests the presence of a room and a corridor located a few meters from the external wall of the monument [35,37,38,62]. These data are in agreement with our analyses which predict, at that point, the presence of a room as a link between the two ramps 1 and 4 of our 3D model. The microgravimetry data, carried out on the pyramid by different research groups [32,33,35,36], can show us how, under the floor of the King's room, there is a lack of homogeneity possibly attributable to structures such as those hypothesized by us (see points 12 and 13 of the 3D model). The presence of rooms located under the King's room is also amply documented by many photographic finds on the Web. The presence of ramps, placed inside the pyramid and which we highlight with certainty for the first time (numbers 1, 2, 3, and 4 of the 3D model), had already been postulated [11] and partly detected by electrogravitic measurements carried out in 1998 [34]. The presence of further rooms located near the Queen's room had already been postulated in the past by some researchers [34,63], based on intuitions not confirmed, however, by objective evidence. Authors of [63] also postulated the presence

Preprints (www.preprints.org) | NOT PEER-REVIEWED | Posted: 18 August 2022 doi:10.20944/preprints202208.0329.v1

of a horizontal passage placed between the original entrance of the pyramid and the Great Gallery, in place of structure number 17 which we highlight in this work; moreover, in this work, the presence of a room located immediately after the entrance to the great pyramid is highlighted. This void also seemed to be confirmed by muon spectroscopy [64] carried out by researchers at the University of Nagoya in 2017 and indicated with the name of "Small Void". It must be strongly emphasized that, while the analyses used up to now in the attempt to describe the objects inside the pyramid, gave only the possibility of making indirect hypotheses, the SAR methodology visibly produces direct evidence of the geometries inside the objects that can be analyzed. In contrast, the muon spectroscopy used in 2017 [64] would not have been deemed reliable by the Egyptian Supreme Council of Antiquities, providing controversial data [40]. No trace of the presence of a structure identified as a Big Void, put in evidence by muonic spectroscopy [64], was in our hands detected by SAR. On the other hand, the SAR technique, allows us of making more observations using different starting geometries, thus being able to see the same structures inside the pyramid, from different points of view, and the only possibility of mistake lies in the visual interpretation of the data obtained but does not invalidate the presence or absence of specific structural elements. The geometries of the objects highlighted by the SAR in this paper, also make us reasonably exclude any errors due to the possible non-homogeneity of the materials employed during the construction of the pyramid interiors.

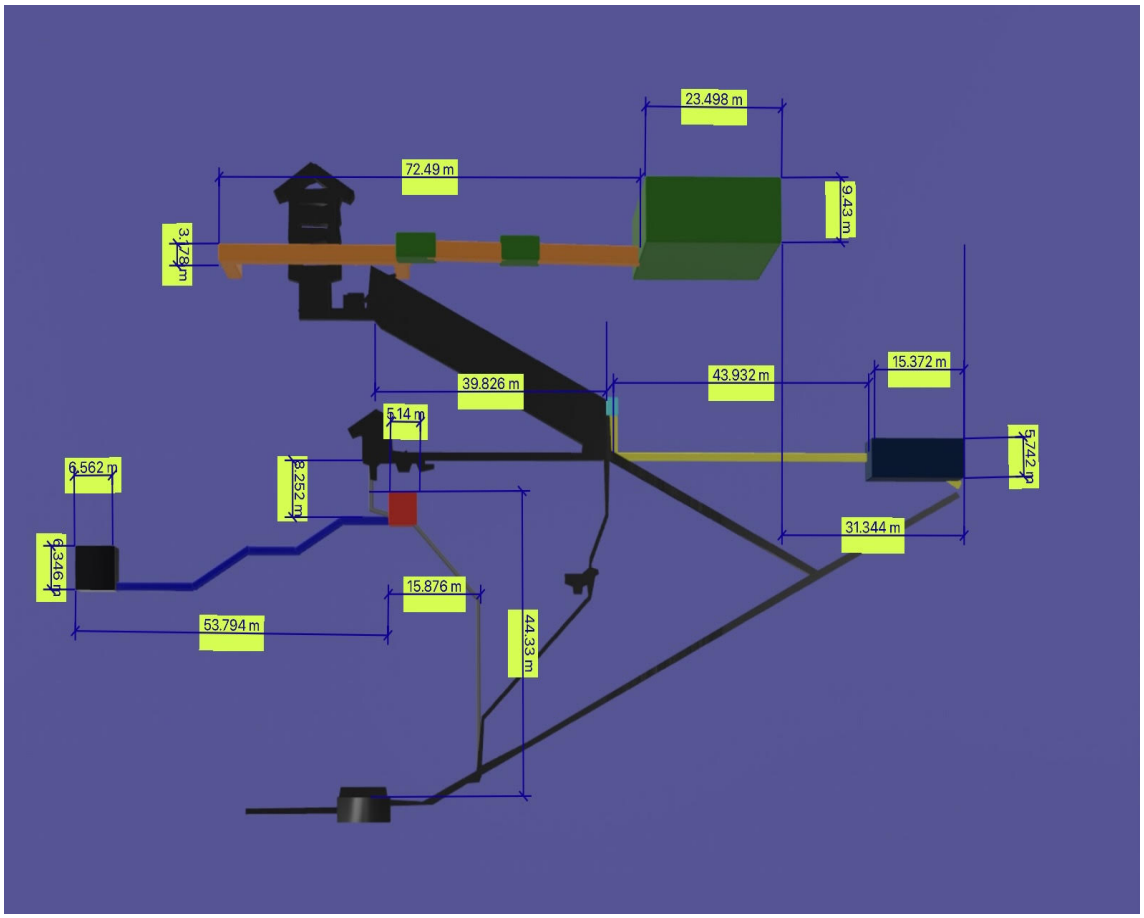

Figure 52. Measurements of the detected facilities of the pyramid. The numbers shown after the comma can not be significant.

8.2. Data interpretation

On the basis of the above, it appears necessary to provide a plausible explanation as a key to understanding the function of the structures found inside the pyramid, taking into account that this interpretation is only intended to be a starting point for further interpretative ideas that could arise

 doi:10.20944/preprints202208.0329.v1

from a serene discussion at the level of the scientific community. The authors' vision starts from what we have already previously published in [65] and widely discussed [8,12,18,19,24,27–30]. Starting from the observation of the outside of the three pyramids of the Giza plateau, for the first time, we were able to establish that the three pyramids of Khnum-Khufu, Kefren and Menkaure have eight sides. This feature, known only for the larger pyramid, is now extended to the other two. According to the authors of [40], the idea that the pyramids of the Giza plateau had this characteristic is due to the need to convey, in an orderly manner, the water that flowed along the faces of the pyramidal structures. In the case of the pyramid of Khnum-Khufu, which we have analyzed in depth, it can be assumed, in analogy with other authors [5,21,66], that it was surrounded by an enormous basin full of water, which allowed the circulation of some boats. These boats were used by some attendants with the task of bringing the water to about 90 meters high, pouring it into the South shaft by using many rotating stones probably similar to the Sabu diorite stone [24]. The SAR tecnique allows us to put in evidence that the shape of this monument do not resemble a perfect pyramidic form because the presence of a double changing in slope: the first of which of 14.5 ca. degrees at approximately 20 meters of high and the second one of 6 degrees ca. at approximately 100 meters of high. The Nile river's water should have filled the basin up to the height of the first change of slope of the pyramid, thus allowing the Egyptian boats not to get stuck with the keel on the side of the pyramid itself The water would have invaded the King's chamber but having reached the height of the granite basin inside the chamber (often referred to as the sarcophagus), it would not have exceeded that level in height and would have instead risen in the North shaft, whose entrance is placed at the same height as the basin, creating an air seal that effectively airlocked the room. The King's chamber in fact hermetically sealed would have caused excess water to rise up the North shaft. The Queen's chamber would also be filled with water, up to the height of the shafts, by means of two connections to the shafts of the King's chamber, probably located in rooms 19 and 11, building a closed circuit, called Quincke's tube [22]. As also proposed by other authors [67], the pyramid, with its megalithic structure was placed in vibration by the wind and the low frequencies thus developed, which acted as a low pass filter allowing only low frequencies to bounce back on the roof of the Zed towards the King's chamber [12]. Such a room would behave like an air-filled bottle of Helmholtz [25], in which the granite basin acted as a bottleneck. The walls of the basin, vibrating at low and precise frequencies, linked to the internal and external measurements of the basin itself, proportional to multiples of π and the Golden Ratio ϕ [12], would have caused the water contained in the Quincke's circuit to vibrate. These frequencies, traveling through the closed circuit of Quincke's tube, at about 1400 m/sec, (speed of sound in the water), reached the Queen's chamber, where the height of the water could not exceed the height of shafts from the floor. A particular frequency could be developed, suitably amplified by the correct dimensions of the niche present in the West wall, which acted as a sound box for a musical instrument, releasing into the air a sound frequency that was able to interact with a cylindrical container, placed on the floor of the room, traces of which are still visible [10]. This cylindrical container, probably made of wood, was put into resonance by the obtained low frequency. Two individuals were placed both in the basin of the King's chamber and in the cylindrical container, in the Queen's chamber and appropriately treated with this low sound frequency for curative and religious purposes [17]. At the end of the procedure, the King's chamber was emptied by letting the water out of the Great Gallery and conveying it towards the room called "Grotto" towards the "Unfinished" chamber which brought the water back through a path in the floor, now occluded by debris, to the Nile. Subsequently, the Queen's chamber was emptied in two steps: first a granite "plug" in the corridor leading to the room was removed: (this passage actually has a slight hydraulic slope towards the Great Gallery) and the water was made to flow out. At the floor of the Great Gallery, where it was conveyed towards the "Grotto". Subsequently, a plug placed in the floor was removed to finish the emptying of the room. The water thus conveyed through the hole in the floor, highlighted in a book published in 1877 [10], allowed the liquid to enter the room which, in our 3D reconstruction, corresponds to the number 14, eventually reaching the "Unfinished" room. and returning to the Nile. The "Grotto" and room 14 are, in

Preprints (www.preprints.org) | NOT PEER-REVIEWED | Posted: 18 August 2022 doi:10.20944/preprints202208.0329.v1

our opinion, necessary to stop the fall of water by slowing down its speed, with a mechanism similar to a common water jet pump used in laboratories to create vacuum in equipment, called Venturi's tube. The evident traces of erosion due to water inside the pyramid rooms are in support of our interpretative hypothesis. The three boulders that today are wedged at the beginning of the oblique corridor leading to the Great Gallery, would have been used as "plugs" to block the access of water to the exit of the pyramid or from the Queen's chamber by making them flow in different positions as needed. The existence of a passage 18 seems to be related with a little open room, never described by anyone but well tracked by numerous photographic evidences, that appears located at the top of the entrance of the Great Gallery, probably employed as security exit. The entire system of the ramps highlighted by the SAR could be interpreted as a gigantic resonant structure, having the purpose of equalizing any differences in vibration between the North and South part of the pyramid, with the aim of making the square structure reach number 10, placed around the Zed, an equalized vibrational signal. Similarly, the complex structure number 9 identified immediately below the plane on which the pyramid rests, has a shape similar to structures used to absorb the effects of mechanical vibrations that are transmitted through the ground [26].

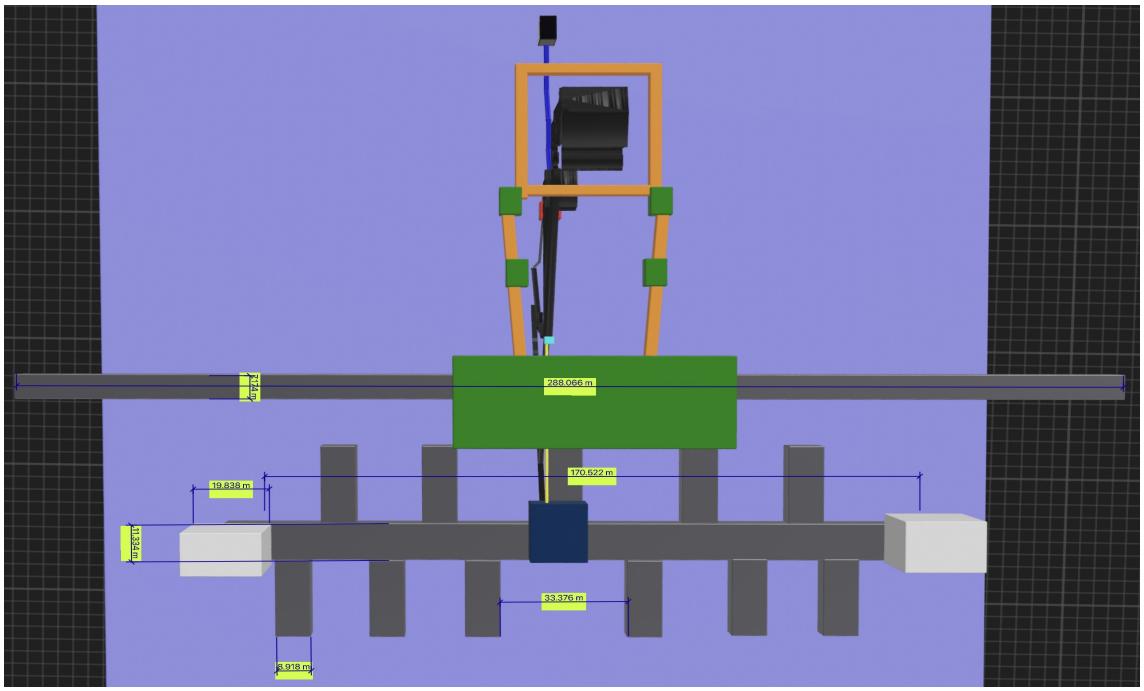

Figure 53. Measurements of the detected facilities of the pyramid. The numbers shown after the comma can not be significant.

9. Acknowledgments

We would like to thank Prof. Daniele Perissin for making the SARPROZ software available, through which many calculations were carried out more easily and quickly. We also thank the Italian Space Agency for providing the SAR data. We would also like to thank Dr. Riccardo Garzelli for conducting a deep revision of the English language and for having made crucial revisions to the entire article's structure and layout. The signal processing technique presented in this work has been submitted patent application in 04 July 2022, to Commerce Department of Malta, Industrial Property Registrations Directorate, patent application number 4451.

10. Author contributions statement

The authors contributed to all parts of this work

 doi:10.20944/preprints202208.0329.v1

Table 2. List of the principal tomographic images.

Picture	Tomographic looking-direction	Tomographic line orientation
Figure 24	Eastern-side	Vertical
Figure 25	Northern-side	Horizontal
Figure 26	Western-side	Horizontal
Figure 27	Eastern-side	Horizontal
Figure 28	Western-side	Horizontal
Figure 29	Northern-side	Horizontal
Figure 30	Western-side	Vertical
Figure 31	Eastern-side	Vertical investigation
Figure 32	Northern-Southern-side	Vertical
Figure 33	Southern-side	Horizontal

Table 3. Characteristics of the SAR acquisitions.

Structure number	Structure type	Structure name
1	Corridor	Eastern ascending ramp
2	Corridor	Western ascending ramp
3	Corridor	Southern Corridor
4	Corridor	Eastern descending ramp
5	Corridor	Western descending ramp
6	Corridor	Northern underground corridor
7	Corridor	Northern-East underground corridor
8	Corridor	Northern-West underground corridor
9	Complex structure	Northern underground complex-structure
10	Complex structure	ZED complex-structure
11	Room	Eastern sarcophagus passage facility
12	Room	Western sarcophagus passage facility
13	Room	Bottom sarcophagus room facility
14	Room	Queen's bottom room
15	Room	Southern bottom room
16	Corridor	Southern Connection
17	Room	Little-void
18	Corridor	Front corridor
19	Room	Big-void
20	Complex structure	ZED-Big-void double connection

11. Conclusions

In this paper we have shown how it is possible to use SAR micro-motion Doppler tomography in an advantageous, economical, non-invasive and rapid way to make a valid contribution in the study of the structure of ancient megalithic monuments such as the pyramid of Khnum-Khufu. We are aware that only by confirmation on the field of our findings can we validate our hypothesis. However it seemed logical to provide a hypothetical interpretation based on the data we collected that could serve as a starting point for future research. In the near future we would like to extend the SAR methodology to the investigation of the internal structure of other important monuments of the Giza plateau.

1. Lehner, M.; Wilkinson, R.H. *Complete Pyramids: Solving the Ancient Mysteries*; Thames and Hudson Incorporated, 1997.
2. Hawass, Z. Pyramid construction: new evidence discovered in Giza. *Stationen: Beiträge zur Kulturgeschichte* **1998**.

3. Smith, C.B.; Hawass, Z. *How the great pyramid was built*; Smithsonian Institution, 2018.
4. Tallet, P.; Marouard, G. The harbor facilities of king Khufu on the Red Sea shore: the Wadi al-Jarf/Tell Ras Budran system. *Journal of the American Research Center in Egypt* **2016**, pp. 135–177.
5. Bhatt, U. SUBCONTINENT OF INDIA: A PART OF THE EARLIEST AND MOST ADVANCED CIVILISATION OF THE WORLD **2019**.
6. Bergendorff, S. *The Social and Cultural Order of Ancient Egypt: An Ethnographic and Regional Analysis*; Lexington Books, 2019.
7. Noc, E. Analyse spatiale à Saqqâra des origines à la fin de l'Ancien Empire: les exemples des complexes funéraires de Netjerikhet et de Sekhemkhet. PhD thesis, Montpellier 3, 2015.
8. Barsoum, M.; Ganguly, A.; Hug, G. Microstructural evidence of reconstituted limestone blocks in the Great Pyramids of Egypt. *Journal of the American Ceramic Society* **2006**, *89*, 3788–3796.
9. Harrell, J.A.; Penrod, B.E. The great pyramid debate–Evidence from the Lauer sample. *Journal of Geological Education* **1993**, *41*, 358–363.
10. Smyth, C.P. *Our inheritance in the Great Pyramid*; London: W. Isbister, 1877.
11. Tasellari, A.; Kaiku, E. How the Great Pyramid of Giza was built. An Engineering View. International Student Conference of Civil Engineering, 2013.
12. Malanga, C. Cheope la fabbrica dell'immortalità, Spaziointeriore, 2020 **2020**.
13. Hancock, G. *Fingerprints of the Gods*; Random House, 2011.
14. Bedard, A.; Georges, T.; others. Atmospheric infrasound. *Acoustics Australia* **2000**, *28*, 47–52.
15. Gossard, E.E.; Hooke, W.H. Waves in the atmosphere: atmospheric infrasound and gravity waves-their generation and propagation. *Atmospheric Science* **1975**, *2*.
16. De Carlo, M.; Ardhuin, F.; Le Pichon, A. Atmospheric infrasound generation by ocean waves in finite depth: unified theory and application to radiation patterns. *Geophysical Journal International* **2020**, *221*, 569–585.
17. Till, R. Sound archaeology: a study of the acoustics of three world heritage sites, Spanish prehistoric painted caves, Stonehenge, and paphos theatre. Acoustics. MDPI, 2019, Vol. 1, pp. 661–692.
18. Henry, S.; Di Borgo, E.P.; Danquigny, C.; Cavaillou, A.; Cottle, A.; Gaffet, S.; Pipe, M. Monitoring geomagnetic signals of groundwater movement using multiple underground SQUID magnetometers. E3S Web of Conferences. EDP Sciences, 2014, Vol. 4, p. 02004.
19. Jouniaux, L.; Ishido, T. Electrokinetics in earth sciences: a tutorial. *International Journal of Geophysics* **2012**, *2012*.
20. Guillaume, C.L.; Gregoryanz, E.; Degtyareva, O.; McMahon, M.I.; Hanfland, M.; Evans, S.; Guthrie, M.; Sinogeikin, S.V.; Mao, H. Cold melting and solid structures of dense lithium. *Nature Physics* **2011**, *7*, 211–214.
21. Zheng, Y.; Ding, L.; Ye, H.; Chen, Z. Vibration-induced property change in the melting and solidifying process of metallic nanoparticles. *Nanoscale Research Letters* **2017**, *12*, 1–11.
22. Hixson, E.; Kahlbau, J. Quincke-Tube Acoustic Filter for Fluid Ducts. *The Journal of the Acoustical Society of America* **1963**, *35*, 1895–1895.
23. Lato, T.; Mohany, A. Passive damping of pressure pulsations in pipelines using Herschel-Quincke tubes. *Journal of Sound and Vibration* **2019**, *448*, 160–177.
24. Hassaan, G.A. Mechanical Engineering in Ancient Egypt, Part XIII: Stone Vessels (Predynastic to Old Kingdom Periods). *International Journal of Recent Engineering Science (IJRES)* **2016**, *19*, 14–24.
25. Liu, X.; Yu, C.; Xin, F. Gradually perforated porous materials backed with Helmholtz resonant cavity for broadband low-frequency sound absorption. *Composite Structures* **2021**, *263*, 113647.
26. D'Alessandro, L.; Belloni, E.; Ardito, R.; Braghin, F.; Corigliano, A. Mechanical low-frequency filter via modes separation in 3D periodic structures. *Applied Physics Letters* **2017**, *111*, 231902.
27. Davidovits, J.; Morris, M. *Why the pharaohs built the Pyramids with fake stones*; Institut Géopolymère, 2009.
28. Mulligan, B.P.; Persinger, M.A. Experimental simulation of the effects of sudden increases in geomagnetic activity upon quantitative measures of human brain activity: validation of correlational studies. *Neuroscience Letters* **2012**, *516*, 54–56.
29. St-Pierre, L.; Parker, G.; Bubenik, G.; Persinger, M. Enhanced mortality of rat pups following inductions of epileptic seizures after perinatal exposures to 5 nT, 7 Hz magnetic fields. *Life Sciences* **2007**, *81*, 1496–1500.

30. Whissell, P.; Persinger, M. Developmental effects of perinatal exposure to extremely weak 7 Hz magnetic fields and nitric oxide modulation in the Wistar albino rat. *International Journal of Developmental Neuroscience* **2007**, *25*, 433–439.
31. Breitner, R.; Houdin, J.P.; Brier, B. A Computer Simulation to Determine When the Beams in the King's Chamber of the Great Pyramid Cracked. *Journal of the American Research Center in Egypt* **2012**, *48*, 23–33.
32. Bui, H.D. *Imaging the Cheops pyramid*; Vol. 182, Springer Science & Business Media, 2011.
33. Lheureux, P. Analyse critique de la rampe interne imaginée par Jean-Pierre Houdin **2010**.
34. Bui, H.; Lakshmanan, J.; Montluçon, J.; Erling, J.; Nakhla, C. The Application of microgravity survey in the endoscopy of ancient monuments. *The Engineering Geology of Ancient Works, Monuments and Historical Sites, Athens* **1988**.
35. Ivashov, S.; Bechtel, T.; Razevig, V.; Capineri, L.; Inagaki, M. A proposed radar method for non-destructive investigation of Egyptian pyramids. *Insight-Non-Destructive Testing and Condition Monitoring* **2021**, *63*, 12–19.
36. Yoshimura, S. Non-Destructive Pyramid Investigations (1), By Electromagnetic Wave Method. *Studies in Egyptian Culture* **1987**, *6*, 61.
37. Bross, A.D.; Dukes, E.; Ehrlich, R.; Fernandez, E.; Dukes, S.; Gobashy, M.; Jamieson, I.; La Riviere, P.J.; Liu, M.; Marouard, G.; others. Tomographic Muon Imaging of the Great Pyramid of Giza. *arXiv preprint arXiv:2202.08184* **2022**.
38. Aly, S.; Assran, Y.; Bonneville, A.; ElMahdy, B.; Kouzes, R.T.; Lintereur, A.; Mahrous, A.; Mostafanezhad, I.; Pang, R.; Rotter, B.; others. Simulation Studies of a Novel Muography Detector for the Great Pyramids. *arXiv preprint arXiv:2202.07434* **2022**.
39. Alvarez, L.W.; Anderson, J.A.; El Bedwei, F.; Burkhard, J.; Fakhry, A.; Girgis, A.; Goneid, A.; Hassan, F.; Iverson, D.; Lynch, G.; others. Search for hidden chambers in the pyramids. *Science* **1970**, *167*, 832–839.
40. Morishima, K.; Kuno, M.; Nishio, A.; Kitagawa, N.; Manabe, Y.; Moto, M.; Takasaki, F.; Fujii, H.; Satoh, K.; Kodama, H.; others. Discovery of a big void in Khufu s Pyramid by observation of cosmic-ray muons. *Nature* **2017**, *552*, 386–390.
41. Pašteka, R.; Zahorec, P.; Papčo, J.; Mrlina, J.; Götze, H.J.; Schmidt, S. The discovery of the "muons-chamber" in the Great pyramid; could high-precision microgravimetry also map the chamber? *Journal of Archaeological Science: Reports* **2022**, *43*, 103464.
42. Odah, H.; Abdallatif, T.; El-Hemaly, I.; El-All, E.A. Gradiometer survey to locate the ancient remains distributed to the northeast of the Zoser Pyramid, Saqqara, Giza, Egypt. *Archaeological Prospection* **2005**, *12*, 61–68.
43. Richardson, R.; Whitehead, S.; Ng, T.; Hawass, Z.; Pickering, A.; Rhodes, S.; Grieve, R.; Hildred, A.; Nagendran, A.; Liu, J.; others. The "Djedi" robot exploration of the southern shaft of the Queen's chamber in the great Pyramid of Giza, Egypt. *Journal of Field Robotics* **2013**, *30*, 323–348.
44. Evans, D.L.; Farr, T.G. The use of interferometric synthetic aperture radar (InSAR) in archaeological investigations and cultural heritage preservation. In *Remote sensing in archaeology*; Springer, 2006; pp. 89–102.
45. Chen, F.; Lasaponara, R.; Masini, N. An overview of satellite synthetic aperture radar remote sensing in archaeology: From site detection to monitoring. *Journal of Cultural Heritage* **2017**, *23*, 5–11.
46. Adams, R.E.; Brown, W.E.; Culbert, T.P. Radar mapping, archeology, and ancient Maya land use. *Science* **1981**, *213*, 1457–1468.
47. Brichieri-Colombi, S. A spurred spiral ramp for the great pyramid of giza. *PalArch's Journal of Archaeology of Egypt/Egyptology* **2020**, *17*, 1–20.
48. Biondi, F. COSMO-SkyMed staring spotlight SAR data for micro-motion and inclination angle estimation of ships by pixel tracking and convex optimization. *Remote Sensing* **2019**, *11*, 766.
49. Biondi, F.; Addabbo, P.; Orlando, D.; Clemente, C. Micro-motion estimation of maritime targets using pixel tracking in COSMO-SkyMed synthetic aperture radar data—An operative assessment. *Remote Sensing* **2019**, *11*, 1637.
50. Ullo, S.L.; Addabbo, P.; Di Martire, D.; Sica, S.; Fiscante, N.; Cicala, L.; Angelino, C.V. Application of DInSAR Technique to High Coherence Sentinel-1 Images for Dam Monitoring and Result Validation Through In Situ Measurements. *IEEE Journal of Selected Topics in Applied Earth Observations and Remote Sensing* **2019**, *12*, 875–890.
51. Chen, H.P. *Structural health monitoring of large civil engineering structures*; John Wiley & Sons, 2018.

52. Biondi.; Addabbo, P.; Ullo, S.L.; Clemente, C.; Orlando, D. Perspectives on the structural health monitoring of bridges by synthetic aperture radar. *Remote Sensing* **2020**, *12*, 3852.
53. Biondi, F.; Addabbo, P.; Clemente, C.; Ullo, S.L.; Orlando, D. Monitoring of Critical Infrastructures by Micromotion Estimation: The Mosul Dam Destabilization. *IEEE Journal of Selected Topics in Applied Earth Observations and Remote Sensing* **2020**, *13*, 6337–6351. doi:10.1109/JSTARS.2020.3030977.
54. Biondi, F.; Clemente, C.; Orlando, D. An Atmospheric Phase Screen Estimation Strategy Based on Multichromatic Analysis for Differential Interferometric Synthetic Aperture Radar. *IEEE Transactions on Geoscience and Remote Sensing* **2019**, *57*, 7269–7280. doi:10.1109/TGRS.2019.2912778.
55. Curlander, J.C.; McDonough, R.N. *Synthetic aperture radar: systems and signal processing*; 1991.
56. Raney, R.K. Synthetic Aperture Imaging Radar and Moving Targets. *IEEE Transactions on Aerospace and Electronic Systems* **1971**, *AES-7*, 499–505. doi:10.1109/TAES.1971.310292.
57. Biondi, F.; Addabbo, P.; Clemente, C.; Ullo, S.L.; Orlando, D. Monitoring of Critical Infrastructures by Micromotion Estimation: The Mosul Dam Destabilization. *IEEE Journal of Selected Topics in Applied Earth Observations and Remote Sensing* **2020**, *13*, 6337–6351.
58. Tufillaro, N.B. Nonlinear and chaotic string vibrations. *American Journal of Physics* **1989**, *57*, 408–414.
59. Dodson, A. The Layer Pyramid of Zawiyet el-Aryan: its layout and context. *Journal of the American Research Center in Egypt* **2000**, *37*, 81–90.
60. Baud, M. *Djéser et la IIIe dynastie*; Pygmalion, 2015.
61. Li, B.; Liu, R.; Cong, Q.; Guo, H.; Lin, Q. Stress Superposition Method and free vibration of corner tensioned rectangular thin membranes. *Thin-Walled Structures* **2021**, *159*, 107201.
62. Marini, B. Real time muography simulator for scanpyramids mission. In *ACM SIGGRAPH 2018 Talks*; 2018; pp. 1–2.
63. Blindenberg, V.; Malherbe, A.; Rouhen, C.; Younsi, N. 3D Technology Solves the Mystery of the Great Pyramid.
64. Houdin, J.P. *La construction de la Grande Pyramide*; Vol. 150, 2007.
65. MS Windows NT Kernel Description. https://ilfattostorico.com/2016/10/18/camere-segrete-nella-piramide-di-cheope-i-primi-dubbi/. Accessed: 2010-09-30.
66. Jana, D. The great pyramid debate: Evidence from detailed petrographic examinations of casing stones from the Great Pyramid of Khufu, a natural limestone from Tura, and a man-made (geopolymeric) limestone. Proceedings of the 29th Conference on Cement Microscopy. International Cement Microscopy Association, Quebec City, QC, 2007, Vol. 207, p. 266.
67. LLC, M. MS Windows NT Kernel Description, 1999.